

# Transport Induced by Mean-Eddy Interaction: I. Theory, and Relation to Lagrangian Lobe Dynamics

Kayo Ide<sup>a</sup> and Stephen Wiggins<sup>b</sup>

<sup>a</sup>*Department of Atmospheric and Oceanic Science,  
Center for Scientific Computation and Mathematical Modeling,  
Institute for Physical Science and Technology,  
& Earth System Science Interdisciplinary Center,  
University of Maryland, College Park, USA*

<sup>b</sup>*School of Mathematics, University of Bristol, Bristol BS8 1TW, UK*

---

## Abstract

In this paper we develop a method for the estimation of **Transport Induced by the Mean-Eddy interaction (TIME)** in two-dimensional unsteady flows. The method is built on the dynamical systems approach and can be viewed as a hybrid combination of Lagrangian and Eulerian methods. The (Eulerian) boundaries across which we consider (Lagrangian) transport are kinematically defined by appropriately chosen streamlines of the mean flow. By evaluating the impact of the mean-eddy interaction on transport, the TIME method can be used as a diagnostic tool for transport processes that occur during a specified time interval along a specified boundary segment.

We introduce two types of TIME functions: one that quantifies the accumulation of flow properties and another that measures the displacement of the transport geometry. The spatial geometry of transport is described by the so-called pseudo-lobes, and temporal evolution of transport by their dynamics. In the case where the TIME functions are evaluated along a separatrix, the pseudo-lobes have a relationship to the lobes of Lagrangian transport theory. In fact, one of the TIME functions is identical to the Melnikov function that is used to measure the distance, at leading order in a small parameter, between the two invariant manifolds that define the Lagrangian lobes. We contrast the similarities and differences between the TIME and Lagrangian lobe dynamics in detail. An application of the TIME method is carried out for inter-gyre transport in the wind-driven oceanic circulation model and a comparison with the Lagrangian transport theory is made.

*Key words:* Eulerian Transport, Lagrangian Transport, Mean-Eddy Interaction, Dynamical Systems Approach, Wind-Driven Ocean Circulation

*PACS:* 47.10.Fg, 47.11.St, 47.27.ed, 47.51.+a, 92.05.-x, 92.10.A-, 92.10.ab, 92.10.ah 92.10.ak, 92.10.Lq, 92.10.Ty, 92.60.Bh

---

*Email addresses:* `ide@umd.edu` (Kayo Ide), `S.Wiggins@bris.ac.uk` (Stephen Wiggins).

*URLs:* `http://www.atmos.umd.edu/` ide (Kayo Ide),  
`http://www.maths.bris.ac.uk/people/faculty/maxsw/` (Stephen Wiggins).

## Contents

1	Introduction and motivation	4
2	Mathematical background	5
2.1	Reference state and kinematically-defined Eulerian boundary	6
2.2	Unsteady flow and perturbation theory	8
3	Transport functions for TIME	9
3.1	Derivation of the finite-time TIME functions	9
3.2	Extension over the infinite TIME functions	12
4	Characteristics of TIME	13
4.1	Characteristics along an individual trajectory	13
4.2	Coherency of transport	14
5	Application to a numerical simulation of the wind-driven double-gyre ocean circulation	16
6	Summary and concluding remarks	19
A	Mathematical Background on Perturbation of Trajectories	20
A.1	A Velocity Field Defined by an Analytical Formula	21
A.2	Velocity Field Defined by a Data Set	24
B	Relation to Lagrangian Transport	25
B.1	Overview of Lagrangian transport	25
B.2	Pseudo-lobe dynamics and Lagrangian lobe dynamics	28
	References	31
	List of Tables	33
	List of Figures	34
	Tables	36
	Figures	40

## 1 Introduction and motivation

Lagrangian transport methods are based on following the individual trajectories obtained by solving the original differential equation (ODE) for the particle location starting from a set of initial conditions  $\mathbf{x}_0$  at time  $t_0$ :

$$\frac{d}{dt}\mathbf{x} = \mathbf{u}(\mathbf{x}, t) , \quad (1)$$

where  $\mathbf{u}$  is the velocity field. The geometrical approach of dynamical systems theory is particularly useful when the flow field has Lagrangian coherent structures that separate the flow into distinct regions. Then Lagrangian lobe dynamics describes the transport process between these regions using stable and unstable manifolds of hyperbolic trajectories as (moving) boundaries. The Lagrangian methods have been applied successfully to a number of unsteady geophysical flow problems; for a review, see [1,2]. If the flow is steady, i.e.,  $\mathbf{u}(\mathbf{x}, t) = \bar{\mathbf{u}}(\mathbf{x})$ , the invariant manifolds are stationary and no transport occurs between the regions.

On the contrary, Eulerian-based methods are mainly concerned with the amount of transport across stationary (Eulerian) boundaries without computing individual trajectories. An advantage of Eulerian methods is that they tend to be much less elaborate than Lagrangian methods in terms of computational implementation. The choice for the Eulerian boundaries is generally flexible, unlike the Lagrangian methods.

From the dynamical systems point of view, a parallel development of a method that computes transport across the Eulerian boundary has yet to take place. In this paper we begin the development of such a method. The method makes use of the interaction between the reference (mean) state and the unsteady variability (eddy) as the fundamental mechanism of transport. Hence we refer to it as the **T**ransport **I**nduced by the **M**ean-**E**ddy interaction (TIME). Using a streamline of the reference state as the boundary across which we consider transport, TIME can be thought as a hybrid of Lagrangian and Eulerian methods. Like the Eulerian method, the boundary is stationary. Like the Lagrangian method, the boundary is kinematically defined and there is no TIME in the steady flow without the unsteady eddy component in the velocity. In certain situations we are able to describe the geometrical relationship of TIME along the Eulerian boundaries with Lagrangian lobe dynamics.

We require no assumption of incompressibility in our theoretical framework. Therefore the ideas and techniques of the TIME method can be applied to two-dimensional compressible flow or three-dimensional volume-preserving flow which can be represented as special classes of two-dimensional flows, such as

the shallow-water model. Remarks concerning incompressibility are provided throughout the paper as special cases. Extensions to three-dimensional flow are possible [3], but there is more complexity in the geometry of the transport, and this will be the topic of a future publication.

The outline of this paper is as follows. In Section 2, we provide a brief mathematical background and introduce the notion of a kinematically-defined Eulerian boundary; readers who are familiar with elementary dynamical systems theory may omit this section without significant loss of continuity by referring back to the notation and definitions as necessary. A brief glossary is also provided in Table 1. The TIME method is defined in Section 3, along with the two types of TIME functions. These functions, along with the notion of pseudo-lobes, are further explored in Section 4. An application of the TIME method is carried out in Section 5 for the inter-gyre transport in the double-gyre ocean circulation model and a comparison with Lagrangian transport theory is presented. Appendix A.1 provides details of perturbation theory, and Appendix B compares the TIME method with the Lagrangian transport methods.

[Tab.1]

While in this paper we focus on introducing and developing the two TIME functions that estimate the amount and the geometry of transport, in the companion paper [4], we expand the TIME method further as a diagnostic tool for transport processes by analyzing in detail the influence of the mean-eddy interaction.

## 2 Mathematical background

In this section, we introduce the basic mathematical background necessary to develop the TIME method. The starting point is first expressing the velocity field (1) in the following form:

$$\mathbf{u}(\mathbf{x}, t) = \overline{\mathbf{u}}(\mathbf{x}) + \mathbf{u}'(\mathbf{x}, t) \quad (2)$$

where  $\overline{\{\cdot\}}$  and  $\{\cdot\}'$ , respectively, correspond to the steady reference state and the unsteady fluctuation around the reference state. The choice of reference state may not be unique. We choose the time-average (mean) of the full time-dependent field as the reference state in this study because the mean-eddy decomposition is natural when the flow field is given by a data set; the TIME method itself does not require the reference state to be the mean. Many of our results will be perturbative in nature, with the (small) perturbation parameter being the amplitude of the fluctuation that is implicitly included in  $\mathbf{u}'(\mathbf{x}, t)$  with respect to  $\overline{\mathbf{u}}(\mathbf{x})$ . Appendix A gives results on the length of time intervals

on which perturbed trajectories remain close to trajectories of the reference state. These results will provide the validity of the perturbative nature of our method since the TIME functions that we derive will be of the form of integrals along perturbed trajectories and approximations that, in principle, can be analytically computed are of the form of integrals along trajectories of the reference state. The regularity assumptions required on the velocity field are minimal. Essentially, we need existence and uniqueness of fluid particle trajectories, the ability to linearize about points in space, compute Taylor expansions through second order with respect to parameters, and for certain integrals of components of the velocity field along trajectories of the reference velocity field to exist. Assuming that the velocity field is twice continuously differentiable with respect to the spatial coordinates, time, and any parameters is adequate. No further assumptions on the nature of the time dependence (e.g. time periodicity, quasiperiodicity, etc.) are required.

The use of perturbation theory in the development of the TIME method is made more transparent if we introduce an "order parameter",  $\varepsilon$ , associated with the fluctuation term as follows:

$$\mathbf{u}'(\mathbf{x}, t) = \varepsilon \hat{\mathbf{u}}(\mathbf{x}, t) \quad (3)$$

where  $|\mathbf{u}'(\bar{\mathbf{x}}^C(s), t)| = \mathcal{O}(\varepsilon |\bar{\mathbf{u}}(\bar{\mathbf{x}}^C(s))|)$ . The introduction of  $\varepsilon$  in this way makes perturbation arguments more transparent. However, the TIME functions can be equally as well expressed in terms of  $\mathbf{u}'(\mathbf{x}, t)$  or  $\varepsilon \hat{\mathbf{u}}(\mathbf{x}, t)$ , but in either case the approximation is to leading order in the size of the fluctuation.

## 2.1 Reference state and kinematically-defined Eulerian boundary

We refer to a curve as Eulerian if it is stationary. The TIME method uses an Eulerian curve  $C = \{\bar{\mathbf{x}}^C(s)\}$  that is defined kinematically as a streamline of the reference flow. It can be given as a solution of

$$\frac{d}{ds} \bar{\mathbf{x}}^C(s) = \bar{\mathbf{u}}(\bar{\mathbf{x}}^C(s)) \quad (4)$$

with an initial condition  $\mathbf{x}_0 = \bar{\mathbf{x}}^C(s_0)$  at time  $t_0$ . For  $C$  to be a physically meaningful boundary,  $\bar{\mathbf{x}}^C(s_0)$  must be a regular point of  $\bar{\mathbf{u}}(\mathbf{x}_0)$ , i.e.,  $|\bar{\mathbf{u}}(\mathbf{x}_0)| \neq 0$ .

A trajectory with an initial condition  $\bar{\mathbf{x}}^C(s_0)$  at time  $t_0$  reaches  $\bar{\mathbf{x}}^C(s_0 - t_0 + t)$  at time  $t$  in the reference flow. This trajectory is uniquely identified by a scalar,  $s_0 - t_0$ , because time shifts of a trajectory remain on the same trajectory in the

reference flow. Throughout the paper, we interpret the *flight-time coordinate variable*  $s$  strictly as a spatial coordinate variable along  $C$  while  $t$  is a temporal variable. Accordingly  $(\bar{\mathbf{x}}^C(s), t) = (\bar{\mathbf{x}}^C(s_0 - t_0 + t), t)$  and

$$(s, t) = (s_0 - t_0 + t, t) \quad (5)$$

can be viewed as different parametrizations of the same trajectory, which we call the *reference trajectory*. The Cartesian pair of coordinates  $(s, t)$  will prove to be particularly convenient for describing the TIME method. A glossary is provided in Table 1 for the principal definitions.

A hyperbolic stagnation point is a singular point. In the reference flow, it is a special trajectory called the *distinguished hyperbolic trajectory* (DHT) [5] and we denote it by  $\bar{\mathbf{x}}^{\text{dht}}$ , i.e.,  $|\bar{\mathbf{u}}(\bar{\mathbf{x}}^{\text{dht}})| = 0$ . Although  $\bar{\mathbf{x}}^{\text{dht}}$  itself cannot be a physically meaningful Eulerian boundary  $C$ , the unstable and stable invariant manifolds that have a DHT at the starting and end point, respectively, are special types of  $C$ :

$$\bar{W}^U = \{\bar{\mathbf{x}}^U(s) \mid \lim_{s \rightarrow -\infty} \bar{\mathbf{x}}^U(s) = \bar{\mathbf{x}}^{\text{dht}}\}; \quad (6a)$$

$$\bar{W}^S = \{\bar{\mathbf{x}}^S(s) \mid \lim_{s \rightarrow \infty} \bar{\mathbf{x}}^S(s) = \bar{\mathbf{x}}^{\text{dht}}\}, \quad (6b)$$

where  $\bar{W}$  denotes the reference manifold with the superscripts  $\{\cdot\}^U$  and  $\{\cdot\}^S$  for unstable and stable invariant manifolds, respectively. In a case where  $\bar{W}^U$  and  $\bar{W}^S$  coincide, the reference streamline is called the *separatrix* or *heteroclinic connection* of the upstream DHT  $\bar{\mathbf{x}}_{-\infty}^{\text{dht}}$  and the downstream DHT  $\bar{\mathbf{x}}_{\infty}^{\text{dht}}$ :

$$\bar{W}^H = \{\bar{\mathbf{x}}^H(s) \mid \lim_{s \rightarrow -\infty} \bar{\mathbf{x}}^H(s) = \bar{\mathbf{x}}_{-\infty}^{\text{dht}}, \lim_{s \rightarrow \infty} \bar{\mathbf{x}}^H(s) = \bar{\mathbf{x}}_{\infty}^{\text{dht}}\}, \quad (7)$$

where the superscript  $\{\cdot\}^H$  stands for heteroclinic connection and the subscripts  $\{\cdot\}_{\mp\infty}$  represent the direction of  $s$  towards the corresponding DHT. In addition, if  $\bar{\mathbf{x}}_{-\infty}^{\text{dht}}$  and  $\bar{\mathbf{x}}_{\infty}^{\text{dht}}$  coincide, then  $\bar{W}^H$  is called the homoclinic connection. An invariant manifold is special case of kinematically-defined  $C$  because  $s$  has a semi-infinite or bi-infinite range as in (6) and (7). We emphasize that the terms *finite* and *infinite* refer to the range of  $s$  on  $C$ , rather than the physical length of  $C$ .

For the description of the transport geometry near  $C$ , it is often convenient to use an orthogonal arc-length coordinate system,  $(l, r)$ . Along  $C$ , the arc-length  $l = l^C(s)$  and the flight-time  $s$  are related by the local velocity, i.e.,

$\frac{d}{ds}l^C(s) = |\bar{\mathbf{u}}(\bar{\mathbf{x}}^C(s))|$ . Normal to  $C$ ,  $r$  is defined to be the signed distance of a neighboring point  $\mathbf{x}$  to  $C$ ;  $r > 0$ ,  $r = 0$  and  $r < 0$  correspond to the left, on, and the right of  $C$  with respect to the forward direction of  $\bar{\mathbf{x}}^C(s)$  along  $C$ . A pair of orthogonal unit vectors in the tangent and normal directions to  $C$  are given by

$$\boldsymbol{\xi}_{\parallel}^C(l^C(s)) = \frac{\bar{\mathbf{u}}(\bar{\mathbf{x}}^C(s))}{|\bar{\mathbf{u}}(\bar{\mathbf{x}}^C(s))|}, \quad \boldsymbol{\xi}_{\perp}^C(l^C(s)) = \frac{(-\bar{u}_2(\bar{\mathbf{x}}^C(s)), \bar{u}_1(\bar{\mathbf{x}}^C(s)))^T}{|\bar{\mathbf{u}}(\bar{\mathbf{x}}^C(s))|}, \quad (8)$$

where  $\mathbf{u} = (u_1, u_2)^T$ . The transformation between the Cartesian and arc-length coordinates is area-preserving.

## 2.2 Unsteady flow and perturbation theory

As we have noted, the mathematical formulation of the TIME method is based on perturbation theory for a velocity field given by (2) and (3). The necessary background and results are given in Appendix A. Trajectories of the unsteady flow passing through  $\mathbf{x}_0$  on  $C$  at  $t_0$  are of the following form:

$$\mathbf{x}(t; \bar{\mathbf{x}}^C(s_0), t_0; \varepsilon) = \bar{\mathbf{x}}^C(s_0 - t_0 + t) + \varepsilon \hat{\mathbf{x}}(t; s_0, t_0) + \mathcal{O}(\varepsilon^2), \quad (9)$$

where  $\varepsilon \hat{\mathbf{x}}(t; s_0, t_0)$  is the leading-order displacement vector with  $\hat{\mathbf{x}}(t_0; s_0, t_0) = 0$ . Computing the Taylor expansion of (2) and the time derivative of (9) with respect to  $\varepsilon$  gives to the following linear ordinary differential equation for  $\hat{\mathbf{x}}(t; s_0, t_0)$ :

$$\frac{d}{dt} \hat{\mathbf{x}}(t; s_0, t_0) = D_{\mathbf{x}} \mathbf{u} \left( \bar{\mathbf{x}}^C(s_0 - t_0 + t) \right) \hat{\mathbf{x}} + \hat{\mathbf{u}}(\bar{\mathbf{x}}^C(s_0 - t_0 + t), t). \quad (10)$$

Given  $C = \{\bar{\mathbf{x}}^C(s)\}$ ,  $\hat{\mathbf{x}}(t; s_0, t_0)$  can be obtained by solving this linear system where the nonlinear evolution of  $\bar{\mathbf{x}}^C(s_0 - t_0 + t)$  provides us with the time-dependent coefficients and the inhomogeneous term. In Appendix A we show that perturbation theory can provide valid approximations in situations where  $C$  is defined over finite, semi-infinite or bi-infinite time intervals.

It is worth noting here that for many of the most fruitful perturbation theories used in dynamical systems type analyses rarely are precise bounds available for the size of the perturbation for which the method is applicable. Nevertheless, this has not limited the insights they have provided in a variety of applications. For example, the typical statements of Melnikov's method [6,7,8] indicate only



that it is valid for  $\varepsilon$  sufficiently small. Another example is the well-known Kolmogorov-Arnold-Moser (KAM) theorem [9], which has been proven useful in many applications despite the fact that the bounds are generally too strict to be practically applicable. The situation with the KAM theorem is even worse since rarely are the hypotheses of the theorem even verified in applications since they require the velocity to be expressed in action-angle variables, which can rarely be achieved. This limitation also prevents one from obtaining any type of bound on the perturbation for which the theorem is valid.

### 3 Transport functions for TIME

Having kinematically defined the Eulerian boundary  $C$  by the reference state, we now turn our attention to transport across  $C$ . There are two aspects: one is concerned with the amount of flow property and the other is concerned with geometry of transport. Examples of flow properties are mass, temperature, humidity in the atmosphere, salinity in the oceans, and such. The TIME functions are developed for these two aspects, first for a finite time interval along any  $C$  (Section 3.1) and then for an infinite time interval along an infinite  $C$  (Section 3.2).

#### 3.1 Derivation of the finite-time TIME functions

##### 3.1.1 Accumulation of a flow property

We assume that the time-dependent fluctuation in the flow property distribution, denoted by  $Q(\mathbf{x}, t)$ , is also small

$$Q(\mathbf{x}, t) = \overline{Q}(\mathbf{x}) + Q'(\mathbf{x}, t) . \quad (11)$$

Like  $\mathbf{u}(\mathbf{x}, t)$  in (2) and (3), we introduce  $Q'(\mathbf{x}, t) = \varepsilon \hat{Q}(\mathbf{x}, t)$  with  $|Q'(\overline{\mathbf{x}}^C(s), t)| = \mathcal{O}(\varepsilon |\overline{Q}(\overline{\mathbf{x}}^C(s))|)$ . To illustrate the basic idea for estimating the amount of property transport, we consider the imaginary fluid column  $\mathcal{F}$  in the flow (Figure 1c). By accumulating the flux at the moving intersection of  $\mathcal{F}$  with  $C$ , we obtain the net amount of accumulation.

[Fig.1]

Up to leading order, the intersection  $(s, t)$  of  $\mathcal{F}$  with  $C$  at time  $t$  is approximated by the reference trajectory  $(s_0 - t_0 + t, t)$  using perturbation theory (Appendix A.1). At  $(s, t)$ , the instantaneous flux of  $Q(\overline{\mathbf{x}}^C(s), t)$  carried by the local velocity  $\mathbf{u}(\overline{\mathbf{x}}^C(s), t)$  across  $C$  per unit length is

$$\begin{aligned} & \xi_{\perp}^C(l^C(s)) \cdot [ Q(\bar{\mathbf{x}}^C(s), t) \mathbf{u}(\bar{\mathbf{x}}^C(s), t) ] = \\ & \xi_{\parallel}^C(l^C(s)) \wedge [ \bar{Q}(\bar{\mathbf{x}}^C(s)) \varepsilon \hat{\mathbf{u}}(\bar{\mathbf{x}}^C(s), t) + \varepsilon^2 \hat{Q}(\bar{\mathbf{x}}^C(s), t) \hat{\mathbf{u}}(\bar{\mathbf{x}}^C(s), t) ] , \end{aligned} \quad (12)$$

where  $\xi_{\perp}^C(l^C(s))$  and  $\xi_{\parallel}^C(l^C(s))$  are defined in (8). The positive value means the flux from the right to the left across  $C$  with respect to the forward direction of  $s$ . This formula (12) says that the instantaneous flux of  $Q$  across  $C$  exists if  $\mathbf{u}(\mathbf{x}, t)$  has a component normal to  $C$ , and that the time-dependent fluctuation  $Q'(\mathbf{x}, t) = \varepsilon \hat{Q}(\mathbf{x}, t)$  contributes to the transport at the higher order. At the leading order, the instantaneous flux of  $Q$  penetrating across  $C$  at  $(s, t)$  per unit flight time is  $\bar{Q}(\bar{\mathbf{x}}^C(s)) \bar{\mathbf{u}}(\bar{\mathbf{x}}^C(s)) \wedge \varepsilon \hat{\mathbf{u}}(\bar{\mathbf{x}}^C(s), t)$ , i.e.,

$$\bar{Q}(\bar{\mathbf{x}}^C(s)) \bar{\mathbf{u}}(\bar{\mathbf{x}}^C(s)) \wedge \mathbf{u}'(\bar{\mathbf{x}}^C(s), t) = \bar{q}^C(s) \mu^C(s, t) \quad (13a)$$

using (3), where

$$\bar{q}^C(s) \equiv \bar{Q}(\bar{\mathbf{x}}^C(s)) \quad (13b)$$

$$\mu^C(s, t) \equiv \bar{\mathbf{u}}(\bar{\mathbf{x}}^C(s)) \wedge \mathbf{u}'(\bar{\mathbf{x}}^C(s), t). \quad (13c)$$

We refer to  $\mu^C(s, t)$  as the *instantaneous flux function*, induced by the unsteadiness (eddy) of the velocity through the interaction with the reference (mean) flow. This is the origin of the transport induced by the mean-eddy interaction (TIME) across  $C$ . The sign of  $\mu^C(s, t)$  indicates the direction of the instantaneous flux.

The accumulation over the interval  $[t_0, t_1]$  is thus approximated by  $\int_{t_0}^{t_1} \bar{q}^C(s_0 - t_0 + \tau) \mu^C(s_0 - t_0 + \tau, \tau) d\tau$  up to leading order. Because this amount is the same for any  $(s, t)$  along the reference trajectory with  $s - t = s_0 - t_0$ , we obtain a general form of the accumulation

$$m^C(s, t; t_0 : t_1) \equiv \int_{t_0}^{t_1} \bar{q}^C(s - t + \tau) \mu^C(s - t + \tau, \tau) d\tau , \quad (14)$$

where the first pair  $(s, t)$  in the arguments of the left-hand side represents the combination of spatial coordinate and time at which the net accumulation of  $Q$  is evaluated, while the next pair  $(t_0 : t_1)$  concerns the time interval on which the transport takes place. Here  $t$  can be either before or after  $t_0$  or  $t_1$ . We refer to  $m^C(s, t; t_0 : t_1)$  as the *accumulation function*. Characteristics of  $m^C(s, t; t_0 : t_1)$  will be discussed further in Section 4.

### 3.1.2 Displacement distance and area

For the geometry, we consider the displacement distance of the particle starting from  $(s_0, t_0)$  on  $C$ . In the unsteady flow at time  $t$ , the displacement of the particle from  $\bar{\mathbf{x}}^C(s_0 - t_0 + t)$  is  $\mathbf{x}'(t; \bar{\mathbf{x}}^C(s_0), t_0)$  up to leading order by (10). For particle transport and its geometry, we choose to use arc-length coordinates  $(l, r)$  in the description of the displacement functions because the displacement distance has the physical dimension of length. Using (9) along a reference trajectory  $(s, t) = (s_0 - t_0 + t)$  with the initial condition  $(l_0, t_0) = (l^C(s_0), t_0)$ , the leading order term for the displacement distance due to particle transport at  $t \in [t_0, t_1]$  is given by

$$r'(t; l_0, t_0) \equiv \xi_{\parallel}^C(l^C(s_0 - t_0 + \tau)) \wedge \mathbf{x}'(t; s_0, t_0) . \quad (15a)$$

Because  $\mathbf{x}'(t; s_0, t_0) = \varepsilon \hat{\mathbf{x}}(t; s_0, t_0)$  can be obtained by solving (10), then so can  $r'(\tau; l_0, t_0)$  by the direct substitution. However, a simpler formula is available by considering

$$a'(t; l_0, t_0) \equiv r'(t; l_0, t_0) |\bar{\mathbf{u}}(\bar{\mathbf{x}}^C(s))| = \bar{\mathbf{u}}(\bar{\mathbf{x}}^C(s_0 - t_0 + t)) \wedge \mathbf{x}'(t; s_0, t_0) , \quad (15b)$$

which corresponds to the displacement area per unit  $s$  along  $C$  as shown in Appendix A. Using  $a'(t_0; l_0, t_0) = 0$  for the initial condition, construction, the solution for the displacement area at  $t_1$  is given by

$$a'(t_1; l_0, t_0) = \int_{t_0}^{t_1} \bar{e}^C(s - t + t_1 : s - t + \tau) \mu^C(s - t + \tau, \tau) d\tau , \quad (16)$$

where

$$\bar{e}^C(s : s_0) \equiv \exp\left\{\int_{s_0}^s \text{trace}\{D_{\mathbf{x}} \bar{\mathbf{u}}(\bar{\mathbf{x}}^C(\theta))\} d\theta\right\} \quad (17)$$

reflects the compressibility of the reference flow; for an incompressible flow,  $\bar{e}^C(s : s_0) \equiv 1$ .

Like the accumulation, the displacement area associated with transport over  $[t_0, t_1]$  can be evaluated at  $(l^C(s), t)$  where  $t$  can be before, in, or after the time interval. Conceptually, this is to let  $a'(t_1; l_0, t_0)$  obtained by (16) evolve under the reference flow over an additional time interval  $[t_1, t]$  to take the incompressibility into account. As shown in Appendix A, the final form of the displacement functions is given by

$$\begin{aligned}
a^C(s, t; t_0 : t_1) &= \bar{e}^C(s : s_0 - t_0 + t_1) a'(t_1; l_0, t_0) \\
&= \int_{t_0}^{t_1} \bar{e}^C(s : s - t + \tau) \mu^C(s - t + \tau, \tau) d\tau,
\end{aligned} \tag{18a}$$

$$r^C(l^C(s), t; t_0 : t_1) = \frac{a^C(s, t; t_0 : t_1)}{|\bar{\mathbf{u}}(\bar{\mathbf{x}}^C(s))|}. \tag{18b}$$

As in the case of  $m^C(s, t; t_0 : t_1)$ , the first pair  $(l^C(s), t)$  in the argument represents the spatial coordinate and time at which the function is evaluated, and the next pair correspond to the time interval when transport takes place.

Accordingly over  $[t_1, t_0]$ , the displacement is determined by two contributions: one is from the unsteadiness of the flow measured along  $C$  through the instantaneous flux  $\mu^C(s - t + \tau, \tau)$ , and the other from the compressibility of the reference flow through  $\bar{e}^C(s : s - t + \tau)$ , which may result in compression or expansion of the area. Sign of  $a^C(s, t; t_0 : t_1)$  indicates the directionality of transport across  $C$ .

### 3.2 Extension over the infinite TIME functions

We refer to the accumulation function (14) and displacement distance and displacement area functions (18) as the (*finite*) *TIME functions* because they are defined over a finite time interval and hence the finite range of  $s$  along  $C$ . These TIME functions can be extended over the semi-infinite  $\bar{W}^U$  and  $\bar{W}^S$  and bi-infinite  $\bar{W}^H$ , because the exponential decay of the velocity towards DHTs at the starting or(and) end point(s) guarantees the convergence conditions required for the validity of perturbation theory (Appendix A). The extension of the displacement functions over  $\bar{W}^H$  can be particularly useful since it provides a direct link to the Melnikov function which measures the leading order distance between the *time-dependent* unstable and stable invariant manifolds [6,7,8]. The Melnikov function has been used to study Lagrangian transport, mostly in incompressible flows [10]; also see [2].

The TIME functions for these special  $C$  are as follows. The transport that has happened in the past across  $\bar{W}^U$  can be obtained by extending the TIME functions over a semi-infinite time interval  $(-\infty, t_0]$ :

$$m^U(s, t; t_0) = \int_{-\infty}^{t_0} \bar{q}^C(s - t + \tau) \mu^C(s - t + \tau, \tau) d\tau; \quad (19a)$$

$$a^U(s, t; t_0) = \int_{-\infty}^{t_0} \bar{e}^C(s : s - t + \tau) \mu^C(s - t + \tau, \tau) d\tau; \quad (19b)$$

$$r^U(l^U(s), t; t_0) \equiv \frac{a^U(s, t; t_0)}{|\bar{\mathbf{u}}(\bar{\mathbf{x}}^U(s))|}. \quad (19c)$$

for some  $t_0$ . Similarly, the transport that will happen in the future across the stable manifold  $\bar{W}^S$  can be obtained by extending the TIME functions over the semi-infinite interval  $[t_0, \infty)$ :

$$m^S(s, t; t_0) = \int_{t_0}^{\infty} \bar{q}^C(s - t + \tau) \mu^C(s - t + \tau, \tau) d\tau; \quad (20a)$$

$$a^S(s, t; t_0) = \int_{t_0}^{\infty} \bar{e}^C(s : s - t + \tau) \mu^C(s - t + \tau, \tau) d\tau; \quad (20b)$$

$$r^S(l^S(s), t; t_0) \equiv \frac{a^S(s, t; t_0)}{|\bar{\mathbf{u}}(\bar{\mathbf{x}}^S(s))|}. \quad (20c)$$

Finally, the entire transport across the separatrix  $\bar{W}^H$  can be obtained by extending the TIME functions over the bi-infinite interval  $(-\infty, \infty)$ :

$$\begin{aligned} m^H(s, t) &= m^U(s, t; t_0) + m^S(s, t; t_0) \\ &= \int_{-\infty}^{\infty} \bar{q}^C(s - t + \tau) \mu^C(s - t + \tau, \tau) d\tau; \end{aligned} \quad (21a)$$

$$\begin{aligned} a^H(s, t) &= a^U(s, t; t_0) + a^S(s, t; t_0) \\ &= \int_{-\infty}^{\infty} \bar{e}^C(s : s - t + \tau) \mu^C(s - t + \tau, \tau) d\tau; \end{aligned} \quad (21b)$$

$$r^H(l^H(s), t) \equiv r^U(l^H(s), t; t_0) + r^S(l^H(s), t; t_0) = \frac{a^H(s, t; t_0)}{|\bar{\mathbf{u}}(\bar{\mathbf{x}}^H(s))|}. \quad (21c)$$

The displacement area function  $a^H(l^H(s), t)$  for  $\bar{W}^H$  is the same as the so-called Melnikov function.

## 4 Characteristics of TIME

### 4.1 Characteristics along an individual trajectory

The accumulation is obtained by following the individual reference trajectories (Section 3). This leads to the concepts of *invriance* and *piece-wise independence*.

**Invariance of the accumulation function.** Given a fixed time interval  $[t_0, t_1]$ , the accumulation function is *invariant*:

$$m^C(s, t; t_0 : t_1) = m^C(s - t + \tau, \tau; t_0 : t_1) \quad (22)$$

for any  $\tau$ . This invariance implies that each trajectory has perfect memory for the amount of transport. Invariance for the displacement area function:

$$a^C(s, t; t_0 : t_1) = \bar{e}^C(s : s - t + \tau) a^C(s - t + \tau, \tau; t_0 : t_1) \quad (23)$$

is subject to the compressibility factor  $\bar{e}^C(s : s - t + \tau)$  of the reference flow.

**Piece-wise independence.** It is clear in the definition (14) that the time interval  $[t_0, t_1]$  can be broken up into an arbitrary number (say  $K$ ) of pieces:

$$m^C(s, t; t_0 : t_1) = \sum_{k=1}^K m^C(s, t; t_{0,k-1} : t_{0,k}) , \quad (24)$$

where  $\cup_{k=1}^K [t_{0,k-1}, t_{0,k}] = [t_0, t_1]$  with  $t_{0,0} = t_0$  and  $t_{0,K} = t_1$ . This is a *temporal piece-wise independence*. Using (5) along  $(s_0 - t_0 + \tau, \tau)$ , *spatial piece-wise independence* follows naturally by breaking the spatial segment  $[s_a, s_b]$  into  $K$  pieces by  $\cup_{k=1}^K [s_{a,k-1}, s_{a,k}] = [s_a, s_b]$  with  $s_{a,0} = s_a$  and  $s_{a,K} = s_b$  and transforming them into  $K$  temporal pieces with  $[t_{0,k-1}, t_{0,k}] = [t_0 - s_{a,0} + s_{a,k-1}, t_0 - s_{a,0} + s_{a,k}]$  over  $[t_0, t_1] = [t_0, t_0 - s_a + s_b]$ . Because the independence is a characteristics defined for a fixed  $(s, t)$ , both temporal independence and spatial independence hold for the displacement area function  $a^C(s, t; t_0 : t_1)$ .

#### 4.2 Coherency of transport

Geometry of particle displacement leads to the concepts associated with the coherency of transport. Because the geometrical characteristics discussed here hold for any  $C$  over any time interval, we will drop  $[t_0 : t_1]$  from each notation for simplicity after the first appearance as indicated in  $[\equiv \{\cdot\}]$ ; for example,  $r^C(l^C(s), t) [\equiv r^C(l^C(s), t; t_0 : t_1)]$ . When  $C$  is taken as  $\bar{W}^H$ , there is a geometrical relation to Lagrangian transport, which we will treat separately in Appendix B.

For an illustration of transport geometry and coherency, let us consider an imaginary material curve  $\mathcal{R}(t)$  placed initially on  $C$  at time  $t_0$ , i.e.,  $\mathcal{R}(t_0) = \{(l, r) | r = 0\}$  (Figure 1d). In the reference flow,  $\mathcal{R}(t)$  advects along  $C$  without any displacement. In the unsteady flow, velocity normal to  $C$  may let  $\mathcal{R}(t)$

depart from  $C$ . For the transport geometry associated with the TIME method, we define

$$R^C(t) = \{(l, r) | l = l^C(s), r = r^C(l^C(s), t)\} , \quad (25)$$

which is the leading order approximation to  $\mathcal{R}(t)$ .

**Pseudo-primary intersection point (pseudo-PIP) sequence of  $R^C(t)$  and  $C$ .** In the unsteady flow,  $R^C(t)$  may intersect with  $C$  to form a chain of lobe-like structures as shown schematically in Figure 1d. We denote such a ordered sequence of such zeros  $\{s_j^C(t) [\equiv s_j^C(t; t_0 : t_1)]\}$  with

$$s_j^C(t) = \{s \mid a^C(s, t) = 0, s_j^C(t) < s_{j+1}^C(t)\} , \quad (26)$$

where we use the fact that the zeros of  $a^C(s, t) [\equiv a^C(s, t; t_0 : t_1)]$  and those of  $r^C(l, t)$  are identical. Unless the zero is non-degenerate,  $\{s_j^C(t)\}$  is generally identical to the intersection sequence of  $\mathcal{R}(t)$  up to the leading order; see [11] and also Appendix A.1. We call  $\{s_j^C(t)\}$  the *pseudo-primary intersection point (pseudo-PIP)* sequence in contrast to the Lagrangian lobe dynamics for the heteroclinic connection. The term 'primary' is used here to emphasize the analogy of the PIP of Lagrangian lobe counterpart. A pseudo-PIP sequence can be transformed into arc-length coordinate  $l_j^C(t) [\equiv l_j^C(t; t_0 : t_1)]$  so that  $l_j^C(t) \equiv l^C(s_j^C(t))$ . [Fig.2]

**Invariance of pseudo-PIP sequence.** Because the displacement area  $a^C(s, t)$  is invariant subject to the compressibility effect from (23) and the compressibility effect will not change  $\{s_j^C(t)\}$  at given  $t$ ,  $\{s_j^C(t)\}$  is invariant. Each  $s_j^C(t)$  coincide with a reference trajectory, i.e.,

$$(s_j^C(\tau), \tau) = (s_j^C(t) - t + \tau, \tau). \quad (27)$$

**Pseudo-lobe sequence.** We denote the lobe-like structure defined by the segments of  $R^C(t)$  and  $C$  between a pair of two adjacent pseudo-PIPs by  $L_{j,j+1}^C(t) [\equiv L_{j,j+1}^C(t; t_0 : t_1)]$  and call it the *pseudo-lobe*:

$$L_{j,j+1}^C(t) = \{(l, r) \mid r(r - r^C(l, t)) \leq 0, l \in [l_j^C(t), l_{j+1}^C(t)]\} . \quad (28)$$

Its sequence makes the chain-like structure, which we call the *pseudo-lobe sequence*,  $\{L_{j,j+1}^C(t)\}$ . Using  $a^C(s, t)$ , the pseudo-lobe is the area surrounded by  $a^C(s, t)$  and  $C$  between two adjacent pseudo-PIPs. It is worth emphasizing that temporal and spatial piece-wise independence (Section 4.1) holds for the displacement function of each pseudo-lobe individually.

**Signed area.** The size of each pseudo-lobe measures the amount of the locally coherent transport. Its *signed area* is given by:

$$A(L_{j,j+1}^C(t)) = \int_{l_j^C(t)}^{l_{j+1}^C(t)} r^C(l, t) dl = \int_{s_j^C(t)}^{s_{j+1}^C(t)} a^C(s, t) ds. \quad (29)$$

If the flow is incompressible, the area of each lobe is invariant, i.e.,  $A(L_{j,j+1}^C(\tau)) = A(L_{j,j+1}^C(t))$ .

**Directionality of pseudo-lobes.** Each pseudo-lobe represents the amount of fluid particles that go across  $C$  over  $[t_0, t_1]$ . Depending on whether  $R^C(t)$  lies to the left or right of  $C$ ,  $L_{j,j+1}^C(t)$  can be of two types, denoted respectively by  $L^{RC}$  or  $L^{CR}$  corresponding to  $r^C(l, t) > 0$  or  $r^C(l, t) < 0$  for transport across  $C$  from right to left or left to right. Provided all intersections are transverse,  $\{L_{j,j+1}^C(t)\}$  alternated the types between  $L^{RC}$  and  $L^{CR}$  along  $C$ , resulting in a chain structure at any given time.

The geometry associated with transport of  $Q$  can be established conceptually by replacing the displacement area function  $a^C(s, t)$  for  $R^C(t)$  with the accumulation function  $m^C(s, t) [\equiv m^C(s, t; t_0 : t_1)]$  in arc-length coordinates. In the case for mass with  $\bar{q}^C(s) \equiv 1$  where the flow is incompressible, this operation results exactly in the displacement functions of fluid particles,  $m^C(s, t) = a^C(s, t)$ .

## 5 Application to a numerical simulation of the wind-driven double-gyre ocean circulation

In this study we apply the TIME method to the inter-gyre transport in the mid-latitude, wind-driven ocean circulation. The data set is obtained by a numerical simulation of a quasi-geostrophic (QG) 3-layer model in a rectangular basin geometry with free slip boundary conditions [12]. Due to the latitudinal antisymmetric wind-stress curl applied at the ocean surface, the basic circulation pattern in the top layer is a double-gyre structure separated by an eastward jet shooting off from the confluence point of the southward and northward western boundary currents (Figure 3). Driven by this strong jet, the subpolar gyre circulates counterclockwise in the north and the subtropical gyre circulates clockwise in the south. Depending on the value of the parameters such as the viscosity and the wind stress curl, the ocean circulation exhibits a rich time-dependent dynamics [13,14].

[Fig.3]

At a wind stress curl of  $0.165 \text{ dyn/cm}^2$ , the ocean dynamics is nearly periodic with dominant spectral peak at period  $T \approx 151 \text{ days}$  in a  $1000 \text{ km} \times 2000$



km rectangular domain. We choose this flow since the physical interpretation for a flow field close to periodic is more simple and therefore it allows us to focus more on demonstrating our method. It is worth noting again that the method itself does not require time periodicity of the flow. The velocity data set used in this study has a spatial resolution of  $12.5\text{km} \times 12.5\text{km}$  and is saved daily after a 30,000-day spin-up from rest. Figure 3a shows the streamfunction  $\psi(\mathbf{x}, t)$  of the top layer at  $t = t_{944}^*$  when  $\psi(\mathbf{x}, t)$  is close to the reference state  $\bar{\psi}(\mathbf{x})$ . From here on, the subscript in  $t^*$  denotes days after the completion of the spin-up. The most significant region of unsteadiness of the flow lies in the upstream region of the eastward jet near the western boundary, while small-amplitude Rossby waves propagate westward in the entire ocean basin. The Lagrangian transport processes between the two gyres are governed by the lobe dynamics associated with the unstable invariant manifold  $\mathcal{W}^U(t)$  of the upstream DHT on the western boundary and the stable invariant manifold  $\mathcal{W}^S(t)$  of the downstream DHT on the eastern boundary; see Appendices A.1 and B for the definitions and more details of  $\mathcal{W}^U(t)$  and  $\mathcal{W}^S(t)$ . The inter-gyre transport in the top layer was carefully studied by [15] using Lagrangian lobe dynamics methods.

For the comparison with the Lagrangian method, we choose the Eulerian boundary of the TIME method as the bi-infinite, reference heteroclinic connection  $\bar{W}^H = \{\bar{\mathbf{x}}^H(s)\}$  which spans over  $s \in (-\infty, \infty)$  with  $\bar{\mathbf{x}}^H(-\infty) = \bar{\mathbf{x}}_{-\infty}^{\text{dht}}$  on the western boundary and  $\bar{\mathbf{x}}^H(\infty) = \bar{\mathbf{x}}_{+\infty}^{\text{dht}}$  on the eastern boundary (solid line in Figure 3c). It is worth noting again that application of the TIME method is not limited to flows that possess a heteroclinic connection. For the computation of the TIME functions, we choose the location of  $s = 0$  so that  $\bar{\mathbf{x}}^H(0)$  is very close to  $\bar{\mathbf{x}}_{-\infty}^{\text{dht}}$  and  $|\bar{\mathbf{u}}(\bar{\mathbf{x}}^H(0))|$  is exponentially close to zero. Along  $\bar{W}^H$ , the speed  $|\bar{\mathbf{u}}(\bar{\mathbf{x}}^H(s))|$  of the mean jet significantly increases starting near  $\bar{\mathbf{x}}^H(s_J)$ . Geographically  $\bar{\mathbf{x}}^H(s_J)$  is separated from  $\bar{\mathbf{x}}^H(0)$  only by 600m. As  $s$  increases towards the downstream direction,  $\bar{W}^H$  makes a sharp turn in around  $\bar{\mathbf{x}}^H(s_N)$  in the north, followed by the second sharp turn around  $\bar{\mathbf{x}}^H(s_S)$  in the south. Measured in the flight time,  $s_J$ ,  $s_N$ , and  $s_S$  are 110days, 129days, and 174.5days, respectively. In the further downstream direction,  $\bar{W}^H$  extends to the east and exhibits little meandering. After about  $\bar{\mathbf{x}}^H(s_{250}^*)$  with the subscript in  $s^*$  for the flight-time coordinate in days from  $s = 0$ ,  $|\bar{\mathbf{u}}(\bar{\mathbf{x}}^H(s))|$  becomes extremely small. In the region near  $\bar{W}^H$ , the order of the unsteadiness relative to the reference state is small ( $\sim 0.1$ ), supporting the applicability of the TIME method (see Appendix A.2).

Figure 4 shows the instantaneous flux  $\mu^H(s, t)$  on  $\bar{W}^H$  as a Hovmöller diagram [16,17] in the  $(s, t)$  space for  $[0, 500] \times [750, 1250]$ . The signals of  $\mu^H(s, t)$  are periodic in  $t$  with the period  $T$  because of the time-periodic ocean dynamics. For small  $s$ ,  $\mu^H(s, t)$  is always near zero because  $|\bar{\mathbf{u}}(\bar{\mathbf{x}}^H(s))|$  is exponentially small near  $\bar{\mathbf{x}}_{-\infty}^{\text{dht}}$ . Also for large  $s$ ,  $\mu^H(s, t)$  is always almost zero because both

[Fig.4]

$\bar{\mathbf{u}}(\bar{\mathbf{x}}^H(s))$  and  $\mathbf{u}'(\bar{\mathbf{x}}^H(s), t)$  are small there. Most signals of  $\mu^H(s, t)$  are confined in between. Figure 5 shows the four different phases of  $\mu^H(s, t)$  during one period of the ocean oscillation at  $t = t_{944}^*$ ,  $t_{982}^*(= t_{944}^* + T/4)$ ,  $t_{1020}^*(= t_{944}^* + T/2)$ , and  $t_{1058}^*(= t_{944}^* + 3T/4)$ . Downstream propagation of the large signals is seen over  $[s_J, s_N]$  where typically three extremes (one local minimum and two local maxima, or *vice versa*, depending on the phase of the ocean dynamics during  $T$ ) propagate downstream. Over the subsequent segment, upstream propagation of the small signals is observed. These signals are a consequence of the double-gyre ocean dynamics (variability) through the interaction with the reference (mean) flow. In the companion paper [4], we examine the details of the variability in the double-gyre ocean dynamics and its relation to transport processes, while the focus of this paper is on the comparison of the results of the TIME method with those obtained by the Lagrangian lobe dynamics method. For the computation of the TIME functions, it suffices to use  $\mu^H(s, t)$  over a short finite segment rather than the entire  $(-\infty, \infty)$  along  $\bar{W}^H$  because  $\mu^H(s, t)$  decays to zero for both small and large  $s$ . Our results presented here use  $\mu^H(s, t)$  over  $[s_0^*, s_{1000}^*]$ . A straight diagonal line in Figure 4 is an example of the reference trajectory along which the TIME functions are integrated.

[Fig.5]

Figure 6 shows the infinite displacement area functions. By choosing  $t_0 = t$  in (19)-(21),  $a^U(s, t; t)$  is the transport that has already happened in the past of the present time  $t$ ,  $a^S(s, t; t)$  is the transport to happen in the future of  $t$ , and  $a^H(s, t)$  is the net inter-gyre transport over all time. The two properties of the TIME functions (Section 4) are observed in this figure as follows. The temporal piece-wise independence property (24) is observed by  $a^H(s, t) = a^U(s, t; t) + a^S(s, t; t)$  for any  $(s, t)$ . The invariance property (23) is observed by  $a^H(s, t) = a^H(s + \delta, t + \delta)$  for any  $\delta$ .

[Fig.6]

Due to the active  $\mu^H(s, t)$  over the segment  $[s_J, s_S]$ , the displacement area functions have the relation  $a^H(s, t) \approx a^S(s, t; t)$  for  $s < s_J$ . This is because no transport has happened there yet, leading to  $a^U(s, t; t) \approx 0$ . Similarly,  $a^H(s, t) \approx a^U(s, t; t)$  holds for  $s > s_S$  because all transport has occurred already, leading to  $a^S(s, t; t) \approx 0$ . Because the bi-infinite displacement area function is the same as the Melnikov function, an implication of these results to the Lagrangian transport is that the development of the Lagrangian lobes are mainly governed by the flow dynamics between  $\bar{\mathbf{x}}^H(s_J)$  and  $\bar{\mathbf{x}}^H(s_S)$ . The Lagrangian lobes simply advect in the downstream direction of  $\bar{\mathbf{x}}^H(s_S)$  without any further inter-gyre transport activities.

Figure 7 shows the corresponding displacement distance functions,  $r^U(l, t; t)$ ,  $r^S(l, t; t)$ , and  $r^H(l, t)$ , along the arc-length coordinate  $l = l^H(s)$  measured in  $km$ . The displacement distance functions are inversely proportional to the local reference velocity  $|\bar{\mathbf{u}}(\bar{\mathbf{x}}^H(s))|$ . Therefore, the pseudo-lobes defined by the two consecutive zeros of the displacement distance functions (see Appendix B) are stretched and stay near zero around  $s_{116}^*$  where  $|\bar{\mathbf{u}}(\bar{\mathbf{x}}^H(s))|$  is maximum along

$\overline{W}^H$ . Accordingly it is near  $s = s_{116}^*$  that the inverse pseudo-PIP  $s^\otimes(t)$  associated with  $r^U(l^H(s), t)$  and  $r^S(l^H(s), t)$  exists for the pseudo-turnstile mechanism (see Appendix B). This also implies that the turnstile mechanism of the Lagrangian lobe dynamics for the inter-gyre transport occurs near  $\overline{\mathbf{x}}^H(s_{116}^*)$ . In the downstream for large  $s$ , all displacement distance functions show vertically elongated pseudo-lobes due to very small  $|\overline{\mathbf{u}}(\overline{\mathbf{x}}^H(s))|$ . The same phenomenon occurs in the upstream for small  $s$  near the upstream DHT. This is related to the elongated structures of the Lagrangian lobes near the DHTs (Figure 3b).

[Fig.7]

The pseudo-lobes of the bi-infinite displacement function can be used to estimate the amount of the Lagrangian inter-gyre transport carried by the Lagrangian lobes (Appendix B). Table 2 summarizes a quantitative comparison. The area  $\mathcal{A}(\mathcal{L}_{j,j+1}^L(t))$  of the Lagrangian lobe  $\mathcal{L}_{j,j+1}^L(t)$  is computed by the Lagrangian method [15], while the area  $A(L_{j,j+1}^H(t))$  of the pseudo-lobe  $L_{j,j+1}^H(t)$  is computed by (29). Agreement between the two methods is quite good.

[Tab.2]

Clearly the Lagrangian lobe dynamics method provides precise geometry associated with particle transport that the TIME method cannot (compare Figure 3b with Figure 7). The computation of  $\mathcal{W}^U(t)$  and  $\mathcal{W}^S(t)$  using a velocity data set given on a grid can be computationally intensive. As described in [18], it requires sophisticated spatial and temporal interpolation schemes. In Figure 3b,  $\mathcal{W}^U(t)$  and  $\mathcal{W}^S(t)$  have about 5000 and 2000 particles, respectively. With this relatively large number of particles, it is also computationally challenging to preserve the area of each Lagrangian lobe precisely, due to the geometrical complexity of  $\mathcal{W}^U(t)$  and  $\mathcal{W}^S(t)$  as well as the limited accuracy of the numerical schemes. In contrast, the TIME method is extremely efficient in computing the transport because it requires a very small number of the simple operations. In this example, we used only 1001 data points along  $\overline{W}^H$  to compute  $a^H(s, t)$ . Once  $a^H(s, t)$  is obtained, it automatically provides the value  $a^H(s + \tau - t, \tau)$  for any  $(s + \tau - t, \tau)$ .

## 6 Summary and concluding remarks

We have developed a mathematical framework for the estimation of **T**ransport **I**nduced by the **M**ean-**E**ddy interaction (TIME) for flow properties and fluid particles with emphasis on two-dimensional unsteady geophysical flows, without the assumption of incompressibility. The TIME method estimates the amount of Lagrangian transport across the kinematically-defined Eulerian boundary by the appropriately chosen streamline of the reference flow (Section 2). The TIME method is a hybrid combination of Lagrangian and Eulerian methods and is based on the dynamical systems approach. It enables on to analyze unique features of transport that neither the Lagrangian nor Eulerian methods can provide.

By considering two different aspects of transport, we obtain the accumulation function for flow properties, as well as the displacement distance and area functions for fluid particles (Section 3). The dynamical systems approach leads to the useful characteristics such as invariance, independence and coherency of the geometry (Section 4). In the companion paper [4], we develop a framework for the analysis of the transport process in which these characteristics play a key role.

The notion of pseudo-lobes is developed to describe the geometry associated with TIME. When a heteroclinic is used as the Eulerian boundary and the time interval for transport to take place is set over a bi-infinite time interval, the pseudo-lobes are geometrically closely related to the Lagrangian lobes of the associated invariant manifolds. The novel turnstile mechanisms for Lagrangian transport can be carried over in the TIME method by taking the mirror image of the pseudo-lobes in the upstream region of the heteroclinic connection (Appendix B). An application to an oceanic problem and a comparison with the Lagrangian lobe dynamics studied by [15] (Section 5).

The TIME method is designed to augment and supplement Lagrangian and Eulerian transport methods by providing the unique capability to analyze the underlying transport processes, as it will be shown in [4]. The method can be applied to more general cases than the application presented in this paper; the method itself does not require the time periodicity of the flow field or a heteroclinic connection in the reference state. Various applications and extensions of the Eulerian transport theory, including three-dimensionality [3], brings a new point of view and direction to transport studies in geophysical flows.

## Acknowledgements

This research is supported by ONR Grant No. N00014-09-1-0418, (KI) and ONR Grant No. N00014-01-1-0769 (SW). We thank Dr. Ana Mancho for providing us with computational codes used in her studies of transport in the wind-driven double gyre. We also thank Dr. Michal Branicki for providing us with his computational codes and related technical help for the computation of the invariant manifolds.

## A Mathematical Background on Perturbation of Trajectories

In this appendix we give the necessary mathematical background that the TIME functions are valid approximations to the quantities that they mea-

sure to leading order in the size of the fluctuation around the reference state. Essentially, the result that we need is that trajectories of the full, time dependent velocity field are "close", in the sense of the size of the fluctuation, to trajectories of the reference state velocity field on the time intervals of interest. The TIME functions are integrals of functions involving the pieces of the decomposed velocity field, flow properties, and geometrical features of the chosen Eulerian curve  $C$

Two distinct situations need to be considered. One is where the velocity field is defined by an analytical formula, discussed in Section A.1. The other is where the velocity field is defined as a data set, discussed in Section A.2.

### *A.1 A Velocity Field Defined by an Analytical Formula*

In this appendix we collect together the results that we use on the approximation of trajectories of the reference flow by trajectories of the flow consisting of the reference flow and the fluctuations about the reference flow over appropriate time intervals. These results are stated here for completeness and they can be found in a number of references. See, e.g., [19,20,7,8,21,22,6]. These results deal with the case of time-periodic fluctuations. However, the arguments and proofs for aperiodically time-dependent fluctuations are the same and are discussed in [23,2].

First, we recall notation established in Section 2.

The velocity field expressed analytically as the sum of a steady reference state and an unsteady fluctuation is given by:

$$\frac{d}{dt}\mathbf{x} = \mathbf{u}(\mathbf{x}, t) = \bar{\mathbf{u}}(\mathbf{x}) + \varepsilon \hat{\mathbf{u}}(\mathbf{x}, t), \quad (30)$$

(note that the following perturbation results are valid for  $\mathbf{x}$  either two or three dimensional). We denote a trajectory of (30) by:

$$\mathbf{x}(t; \bar{\mathbf{x}}^C(s_0), t_0). \quad (31)$$

The reference velocity field is given by:

$$\frac{d}{ds}\bar{\mathbf{x}}^C(s) = \bar{\mathbf{u}}(\bar{\mathbf{x}}^C(s)), \quad (32)$$

We denote a trajectory of the reference velocity field by:

$$\bar{\mathbf{x}}^C(s_0 - t_0 + t). \quad (33)$$

Basic results in the theory of ordinary differential equations say that if (30) is a  $C^r$  (i.e.  $r$  times continuously differentiable) function of  $t$ ,  $x$ , and  $\varepsilon$ , then (31) is a  $C^r$  function of  $t$ ,  $s$ , and  $\varepsilon$ . Hence, we can Taylor expand in any of those variables.

In particular, (31) can be substituted into (2) and differentiated with respect to  $\varepsilon$ . In this way we obtain ordinary differential equations for the coefficients (which are functions of time) for the different powers of  $\varepsilon$ . Following this procedure, we obtain:

$$\mathbf{x}(t; \bar{\mathbf{x}}^C(s_0), t_0) = \bar{\mathbf{x}}^C(s_0 - t_0 + t) + \varepsilon \hat{\mathbf{x}}(t; s_0, t_0) + \mathcal{O}(\varepsilon^2), \quad (34)$$

where  $\hat{\mathbf{x}}(t; s_0, t_0)$  satisfies the *first variational equation*:

$$\frac{d}{dt} \hat{\mathbf{x}} = D_{\mathbf{x}} \bar{\mathbf{u}}(\bar{\mathbf{x}}^C(s_0 - t_0 + t)) \hat{\mathbf{x}} + \hat{\mathbf{u}}(\bar{\mathbf{x}}^C(s_0 - t_0 + t), t), \quad (35)$$

which is a linear, inhomogeneous, differential equation. It is clear that with more work one could derive differential equations whose solutions are the coefficients of the higher order terms in the  $\varepsilon$  expansion of the trajectories. However, the first order term in  $\varepsilon$  will be sufficient for our purposes.

In order for our results to be valid we will need estimates on the time interval for which (31) and (33) are  $\mathcal{O}(\varepsilon)$  close (as measured in an appropriate norm, say the maximum of the Euclidean distance between the two trajectories over the time interval of interest).

We state our first result on closeness over finite time intervals.

**Proposition A.1 (Finite Time Approximation.)** *Suppose  $|\mathbf{x}(t_0; \bar{\mathbf{x}}^C(s_0), t_0) - \bar{\mathbf{x}}^C(s_0)| = \mathcal{O}(\varepsilon)$ . Then  $|\mathbf{x}(t; \bar{\mathbf{x}}^C(s_0), t_0) - \bar{\mathbf{x}}^C(s_0 - t_0 + t)| = \mathcal{O}(\varepsilon)$  for  $|t - t_0| = \mathcal{O}(1)$ .*

This result is elementary and well-known, and is a consequence of a simple application of Gronwall's inequality that can be found in the references given above, as well as many texts dealing with perturbation results.

In Section 2 we discussed the situation where the (steady) reference flow contained a hyperbolic stagnation point, denoted  $\bar{\mathbf{x}}^{\text{dht}}$ , with the hyperbolic stagnation point having stable and unstable manifolds,  $\bar{W}^U(\bar{\mathbf{x}}^{\text{dht}})$  and  $\bar{W}^S(\bar{\mathbf{x}}^{\text{dht}})$ ,

respectively. We next state a result that describes how this hyperbolic structure persists under perturbation of the reference flow by the fluctuation.

Let  $B_{\varepsilon_0}$  denote the ball of radius  $\varepsilon_0$  centered at  $\bar{\mathbf{x}}^{\text{dht}}$ . Let  $\bar{W}_{\text{loc}}^U(\bar{\mathbf{x}}^{\text{dht}})$  denote the component of the intersection of  $\bar{W}^U(\bar{\mathbf{x}}^{\text{dht}})$  with  $B_{\varepsilon_0}$  that contains  $\bar{\mathbf{x}}^{\text{dht}}$ . Similarly for  $\bar{W}_{\text{loc}}^S(\bar{\mathbf{x}}^{\text{dht}})$ . Then we have the following well-known result.

**Proposition A.2 (Persistence of Hyperbolic Structures)** *There exists  $\varepsilon_0$  sufficiently small such that for all  $0 < \varepsilon \leq \varepsilon_0$  (30) has a hyperbolic (time dependent) trajectory  $\mathbf{x}_\varepsilon^{\text{dht}}(t) = \bar{\mathbf{x}}^{\text{dht}} + \mathcal{O}(\varepsilon)$ . Moreover,  $\mathbf{x}_\varepsilon^{\text{dht}}(t)$  has local stable and unstable manifolds, denoted  $\bar{W}_{\text{loc}}^S(\bar{\mathbf{x}}_\varepsilon^{\text{dht}}(t))$  and  $\bar{W}_{\text{loc}}^U(\bar{\mathbf{x}}_\varepsilon^{\text{dht}}(t))$ , that are  $C^r$   $\varepsilon$  close to  $\bar{W}_{\text{loc}}^S(\bar{\mathbf{x}}^{\text{dht}})$  and  $\bar{W}_{\text{loc}}^U(\bar{\mathbf{x}}^{\text{dht}})$ , respectively.*

Note that it is an "infinite time" result.

Using an argument that combines Proposition A.1 and Proposition A.2, the following result can be proven.

**Proposition A.3 (Approximation on Semi-Infinite Time Intervals)** *Suppose we choose initial conditions of trajectories in the stable and unstable manifolds of the hyperbolic trajectory at  $t = t_0$ :*

$$\mathbf{x}^S(t; \bar{\mathbf{x}}^C(s_0), t_0) \in \bar{W}_\varepsilon^S(\bar{\mathbf{x}}_\varepsilon^{\text{dht}}(t_0)), \quad (36)$$

$$\mathbf{x}^U(t; \bar{\mathbf{x}}^C(s_0), t_0) \in \bar{W}_\varepsilon^U(\bar{\mathbf{x}}_\varepsilon^{\text{dht}}(t_0)) \quad (37)$$

then

$$\begin{aligned} \mathbf{x}^S(t; \bar{\mathbf{x}}^C(s_0), t_0) &= \bar{\mathbf{x}}^C(s_0 - t_0 + t) + \varepsilon \hat{\mathbf{x}}^S(t; s_0, t_0) + \mathcal{O}(\varepsilon^2) \\ &\quad \text{uniformly in } t \text{ for } t \in [t_0, \infty) \\ \mathbf{x}^U(t; \bar{\mathbf{x}}^C(s_0), t_0) &= \bar{\mathbf{x}}^C(s_0 - t_0 + t) + \varepsilon \hat{\mathbf{x}}^U(t; s_0, t_0) + \mathcal{O}(\varepsilon^2) \\ &\quad \text{uniformly in } t \text{ for } t \in (-\infty, t_0] \end{aligned} \quad (38)$$

where  $\hat{\mathbf{x}}^S(t; s_0, t_0)$  and  $\hat{\mathbf{x}}^U(t; s_0, t_0)$  satisfy

$$\begin{aligned}
\frac{d}{dt}\hat{\mathbf{x}}^S &= D_{\mathbf{x}}\bar{\mathbf{u}}(\bar{\mathbf{x}}^C(s_0 - t_0 + t))\hat{\mathbf{x}}^S + \hat{\mathbf{u}}(\bar{\mathbf{x}}^C(s_0 - t_0 + t), t) \quad \text{for } t \in [t_0, \infty), \\
\frac{d}{dt}\hat{\mathbf{x}}^U &= D_{\mathbf{x}}\bar{\mathbf{u}}(\bar{\mathbf{x}}^C(s_0 - t_0 + t))\hat{\mathbf{x}}^U + \hat{\mathbf{u}}(\bar{\mathbf{x}}^C(s_0 - t_0 + t), t) \quad \text{for } t \in (-\infty, t_0],
\end{aligned} \tag{39}$$

Now we give a brief derivation of the integral formula for the displacement area discussed in Section 3.1.2. Writing  $\mathbf{x}'(t; s_0, t_0) = \varepsilon \hat{\mathbf{x}}(t; s_0, t_0)$ ,  $r'(t; l_0, t_0) = \varepsilon \hat{r}(t; l_0, t_0)$  and  $a'(t; l_0, t_0) = \varepsilon \hat{a}(t; l_0, t_0)$ , (15b) takes the form:

$$\hat{a}(t; l_0, t_0) \equiv \hat{r}(t; l_0, t_0) |\bar{\mathbf{u}}(\bar{\mathbf{x}}^C(s))| = \bar{\mathbf{u}}(\bar{\mathbf{x}}^C(s_0 - t_0 + t)) \wedge \hat{\mathbf{x}}(t; s_0, t_0) , \tag{40}$$

Differentiating (40) with respect to  $\tau$  gives

$$\frac{d}{d\tau} \hat{a}(\tau; l_0, t_0) = \text{trace}\{D_{\mathbf{x}}\bar{\mathbf{u}}(\bar{\mathbf{x}}^C(s - t + \tau))\} \hat{a}(\tau; l_0, t_0) + \mu^C(s - t + \tau, \tau) , \tag{41}$$

that has a clear resemblance to (10). Unlike (10) that is two-dimensional for  $\mathbf{x}'(t; s_0, t_0)$ , (41) is a scalar, linear ordinary differential equation and hence can be solved analytically. Doing so with initial condition  $a'(t_0; l_0, t_0) = 0$  gives (16).

## A.2 Velocity Field Defined by a Data Set

When the velocity field  $\mathbf{u}(\mathbf{x}, t)$  is given as a data set, we need to consider more carefully the applicability of the collection of mathematical results discussed above since the data set does not contain an explicit  $\varepsilon$ . Practically, this means we must first decide on a particular decomposition of  $\mathbf{u}(\mathbf{x}, t)$  into  $\bar{\mathbf{u}}(\mathbf{x}, t)$  and  $\varepsilon \hat{\mathbf{u}}(\mathbf{x}, t)$ . Although the choice of  $\bar{\mathbf{u}}(\mathbf{x})$  is not unique, a natural choice is the time average (mean) of  $\mathbf{u}(\mathbf{x}, t)$ . The geometrical structure of the flow defined by  $\bar{\mathbf{u}}(\mathbf{x})$ , we can make a choice for  $C = \{\bar{\mathbf{x}}^C(s)\}$ . The residual becomes the unsteady fluctuation, i.e.,

$$\mathbf{u}'(\mathbf{x}, t) = \mathbf{u}(\mathbf{x}, t) - \bar{\mathbf{u}}(\mathbf{x}, t) . \tag{42}$$

Once a decomposition of the data set is chosen we then need to examine the smallness of  $\mathbf{u}'(\mathbf{x}, t)$  with respect to  $\bar{\mathbf{u}}(\mathbf{x})$ . As in Section 3 and Appendix A.1,



we do so for the separate types of  $C$ : finite time interval, and semi- or bi-infinite time interval.

The essential result required is to show that the unsteady perturbation is actually small for a finite-time interval  $C$ . There are numerous ways of doing this. One way is to consider the quantity:

$$\alpha^C(\mathbf{x}, t) = \frac{|\mathbf{u}'(\mathbf{x}, t)|}{|\bar{\mathbf{u}}(\mathbf{x})|} \quad (43)$$

where  $|\cdot|$  denotes a convenient norm. This quantity can be estimated numerically in a neighborhood of  $C$  for a time interval of interest.

For either a semi-infinite or a bi-infinite time interval,  $\alpha^C(\mathbf{x}, t)$  defined by (43) will not generally be small at the endpoints of  $C$  where we have  $\bar{\mathbf{x}}^{\text{dht}}$  since  $|\bar{\mathbf{u}}(\bar{\mathbf{x}}^{\text{dht}})| = 0$ . However, this does not affect the validity of the TIME functions since the integrand of each function contains  $\bar{\mathbf{u}}(\bar{\mathbf{x}}^C(s_0 - t_0 + t))$  which vanishes exponentially fast as  $\bar{\mathbf{x}}^{\text{dht}}$  is approached along  $C$ . The argument here is the same as the proof of absolute convergence of the Melnikov integrals given in the references at the beginning of this appendix. Effectively, the smallness of (43) only needs to be established along  $C$  outside of a neighborhood of any endpoints of  $C$  that are hyperbolic stagnation points.

## B Relation to Lagrangian Transport

This appendix describes the similarities and differences between the Lagrangian lobe dynamics that is closely associated with the pseudo-lobe dynamics of the TIME method along  $\bar{W}^H$ . All TIME functions used in this section have the superscript  $\{\cdot\}^H$ , reflecting the fact that the Eulerian boundary  $C$  we are considering is  $\bar{W}^H$ . We begin by presenting a brief description of Lagrangian transport from the dynamical systems point of view; details of the theory can be found in [11,23,18,2].

### B.1 Overview of Lagrangian transport

**Geometry of Lagrangian invariant manifolds.** Lagrangian lobes are formed by time-dependent unstable and stable invariant manifolds,  $\mathcal{W}^U(t)$  and  $\mathcal{W}^S(t)$ , of upstream and downstream time-dependent DHTs,  $\mathbf{x}_{-\infty}^{\text{dht}}(t)$  and  $\mathbf{x}_{\infty}^{\text{dht}}(t)$ . The geometry is schematically shown in Figure 8. For convenience, we parameterize the coordinate of the points on  $\mathcal{W}^U(t)$  by  $\mathbf{x}^U(s, t)$  and on  $\mathcal{W}^S(t)$  by  $\mathbf{x}^S(s, t)$ ,

respectively, by the flight-time coordinate  $s$  using their normal projection onto  $\overline{W}^H = \{\overline{\mathbf{x}}^H(s)\}$ , i.e.,  $(\mathbf{x}^{U,S}(s, t) - \overline{\mathbf{x}}^H(s)) \cdot \boldsymbol{\xi}_{\parallel}^C(l^C(s)) = 0$  for both  $\mathcal{W}^U(t)$  and  $\mathcal{W}^S(t)$ . Then the normal distance from  $\overline{W}^H$  to  $\mathcal{W}^U(t)$  and  $\mathcal{W}^S(t)$  is:

$$r_{\perp}^{U,S}(l^H(s), t) = (\mathbf{x}^{U,S}(s, t) - \overline{\mathbf{x}}^H(s)) \wedge \boldsymbol{\xi}_{\parallel}^C(l^C(s)) , \quad (44)$$

where the subscript  $\{\cdot\}_{\perp}$  here represents the normal projection. Accordingly, the normal distance from  $\mathcal{W}^S(t)$  to  $\mathcal{W}^U(t)$  is defined by:

$$r_{\perp}^L(l, t) = r_{\perp}^U(l, t) - r_{\perp}^S(l, t). \quad (45a)$$

The superscript  $\{\cdot\}^L$  stands for Lagrangian. This normal distance  $r_{\perp}^L(l, t)$  is approximated using the so-called Melnikov function up to leading order, which is identical to the displacement distance function of TIME:

$$r_{\perp}^L(l^H(s), t) = \frac{a^H(l^H(s), t)}{|\mathbf{u}(\overline{\mathbf{x}}^H(s))|} = r^H(l^H(s), t). \quad (45b)$$

[Fig.8]

**Principal Intersection Point (PIP) sequence.** An intersection sequence between  $\mathcal{W}^U(t)$  and  $\mathcal{W}^S(t)$  can be expressed as a discrete sequence,  $\{s_j^L(t)\}$  with  $s_j^L(t) < s_{j+1}^L(t)$ . These intersecting points are called principal intersection points (PIPs). The sequence can be transformed to the arc-length coordinates  $\{l_j^L(t)\}$  using  $l_j^L(t) = l^H(s_j^L(t))$ . Invariance of  $\mathcal{W}^U(t)$  and  $\mathcal{W}^S(t)$  guarantees that a trajectory starting at any PIP will remain a PIP for all time. From (45b), the PIP sequence can be approximated by the zero sequence of  $r^H(l^H(s), t)$  up to leading order:

$$s_j^L(t) \sim s_j^H(t), \quad l_j^L(t) \sim l^H(s_j^H(t)). \quad (46)$$

**Lagrangian lobe and its classification by the directionality of transport.** A Lagrangian lobe,  $\{\mathcal{L}_{j,j+1}^L(t)\}$ , is then defined by segments of  $\mathcal{W}^U(t)$  and  $\mathcal{W}^S(t)$  between a pair of adjacent PIPs corresponding to  $s_j^L(t)$  and  $s_{j+1}^L(t)$ . We classify them into the two types,  $\mathcal{L}^{US}$  or  $\mathcal{L}^{SU}$ , depending on whether the corresponding segment of  $\mathcal{W}^U(t)$  lies to the left or to the right of the corresponding segment of  $\mathcal{W}^S(t)$ , where the directionality is measured with respect to the forward direction of  $s$  along  $\overline{W}^H$ .

**Area of a lobe.** Using an elaborate computational scheme, it is possible to compute the area  $\mathcal{A}(\mathcal{L}_{j,j+1}^L(t))$  of  $\mathcal{L}_{j,j+1}^L(t)$  [15]. Using (45b) and (46) as well

as (29) on  $\overline{W}^H$ , leading order approximation of  $\mathcal{A}(\mathcal{L}_{j,j+1}^L(t))$  is given by the Melnikov function [11], which we denote by  $A(\mathcal{L}_{j,j+1}^L(t))$ :

$$\mathcal{A}(\mathcal{L}_{j,j+1}^L(t)) \approx A(\mathcal{L}_{j,j+1}^L(t)) = A(L_{j,j+1}^H(t)) , \quad (47)$$

where  $A(L_{j,j+1}^H(t))$  is given by (29).

**Moving boundary and boundary PIP.** In order to describe Lagrangian transport, a Lagrangian boundary must be defined using the segments of moving invariant manifolds  $\mathcal{W}^U(t)$  and  $\mathcal{W}^S(t)$ :

$$\mathcal{W}^b(t) = \{\mathbf{x}^U(s, t), s \leq s^b(t)\} \cup \{\mathbf{x}^S(s, t), s \geq s^b(t)\}, \quad (48a)$$

where  $s^b(t) \subset \{s_j^L(t)\}$  is called a boundary PIP as schematically shown in Figure 8a. Unlike Eulerian transport with a well-defined stationary boundary  $\overline{W}^H$ , the selection of  $s^b(t)$  out of all the existing PIPs and hence the selection of  $\mathcal{W}^b(t)$  may not be unique. However a physically meaningful choice may be to have  $\mathcal{W}^b(t) = \{\mathbf{x}^b(s, t)\}$  geometrically "close" to  $\overline{W}^H$  [10]. This condition requires smallness of both  $|r_\perp^U(l^H(s), t)|$  and  $|r_\perp^S(l^H(s), t)|$  in the neighborhood of  $s^b(t)$ , and hence smallness of  $|r_\perp^L(l^H(s), t)|$  approximated by  $|r^L(l^H(s), t)|$ . From (45b), a reasonable choice of  $s^b(t)$  is therefore

$$s^b(t) = \{s \in s_j^L(t) \mid \min |l^H(s_{\overline{\mathbf{u}}}) - l^H(s)|\} \quad (48b)$$

where  $s_{\overline{\mathbf{u}}} = \{s \mid \max |\overline{\mathbf{u}}(\overline{\mathbf{x}}^H(s))|\}$  is the maximum velocity point on  $\overline{W}^H$ .

**Further classification of  $\mathcal{L}_{j,j+1}^L(t)$  by the timing of transport.** The relation between  $s^b(t)$  and  $s_j^L(t)$  leads to a further classification of the Lagrangian lobes beyond  $\mathcal{L}^{US}$  or  $\mathcal{L}^{SU}$  that also describes the timing of transport associated with  $\mathcal{L}_{j,j+1}^L(t)$ .

Particles in  $\mathcal{L}_{j,j+1}^L(t)$  with  $s_j^L(t) < s^b(t)$  are yet to cross  $\mathcal{W}^b(t)$  and hence have not involved in the transport process yet. Because where  $\mathcal{W}^b(t)$  is a segment of  $\mathcal{W}^U(t)$ , we classify these Lagrangian lobes as  $\mathcal{L}^{(b=)US}$  and  $\mathcal{L}^{SU(=b)}$  with the same directionality as  $\mathcal{L}^{US}$  or  $\mathcal{L}^{SU}$ , respectively. On the contrary, particles in  $\mathcal{L}_{j,j+1}^L(t)$  with  $s_j^L(t) > s^b(t)$  have crossed  $\mathcal{W}^b(t)$  and hence have already involved in the transport process. We classify these Lagrangian lobes as  $\mathcal{L}^{US(=b)}$  and  $\mathcal{L}^{(b=)SU}$  with the same directionality as  $\mathcal{L}^{US}$  or  $\mathcal{L}^{SU}$ , respectively.

**Discrete transport time sequence.** As particles advect downstream in the unsteady flow,  $s^b(t)$  must change in time not only by advection but also for keeping the shape of  $\mathcal{W}^b(t)$  as close as possible to  $\overline{W}^H$  as defined in (48b).

Accordingly,  $s^b(t)$  must jump from  $s_j^L(t)$  to  $s_{j-\Delta j}^L(t)$  at some discrete time sequence,  $\{t_k^b\}$  where  $j_k^b$  is the corresponding PIP number and  $\Delta j_k^b$  and increment for the  $k$ -th jump. The integer  $\Delta j_k^b$  should be positive so that the shift of  $s^b(t)$  moves towards upstream at  $t_k^b$ . Between two consecutive jumps  $t \in (t_k^b, t_{k+1}^b)$ , there is no Lagrangian transport between the kinematically-distinct regions because they are defined by the same (moving) boundary  $\mathcal{W}_k^b(t)$ . At the discrete time sequence  $\{t_k^b\}$ , Lagrangian transport by the lobe dynamics occur due to the change of the boundary.

**Turnstile mechanism of transport.** At the discrete time sequence  $\{t_k^b\}$ , a total of  $\Delta j_k^b - 1$  lobes,  $\mathcal{L}_{n,n+1}^L(t_k^b)$ , for  $n = (j_k^b - \Delta j_k^b), \dots, (j_k^b - 1)$ , go across  $\mathcal{W}^b(t_k^b)$  into the other region. Therefore, the lobes of  $\mathcal{L}^{(b)=SU}$  turn into  $\mathcal{L}^{US(=b)}$  and those of  $\mathcal{L}^{(b)=US}$  turn into  $\mathcal{L}^{SU(=b)}$ . This is the so-called turnstile mechanism. As a consequence, Lagrangian transport involves only a few lobes at a time that are spatially confined near the time-dependent boundary point  $(s^b(t_k^b), t_k^b)$ .

## B.2 Pseudo-lobe dynamics and Lagrangian lobe dynamics

The turnstile mechanism of the Lagrangian method is crucial in understanding the transport of particles between the kinematically-distinct regions across the invariant boundary  $\mathcal{W}^b(t)$ . Lagrangian transport occurs locally only near  $\bar{\mathbf{x}}^H(s^b(t_k^b), t_k^b)$  as above. at the discrete time sequence  $\{t_k^b\}$ . Therefore each Lagrangian lobe  $\mathcal{L}_{j,j+1}^L(t)$  can be classified decisively whether transport associated with it has occurred or not, by its relative position with respect to the  $s^b(t)$ .

Table 3 presents a general comparison between the TIME and the Lagrangian method. The TIME method computes the net amount of transport over time across a stationary Eulerian boundary  $C$ . At time  $t$ , pseudo-lobes  $\{L_{j,j+1}^C(t)\}$  may contain a mixture of transport that occurred in the past and in the future. This effect particularly manifests itself along the heterolonic connection  $\bar{W}^H$ , for the past  $(-\infty, t]$  and the future  $\tau \in [t, \infty)$ . This is because the transport boundary is fixed as  $\bar{W}^H$  unlike  $\mathcal{W}^b(t)$ , which changes from  $\mathcal{W}^U(t)$  to  $\mathcal{W}^S(t)$  at  $s^b(t)$ . Therefore the TIME method by itself does not present such a mechanism because it deals with the net amount of transport over time but not individual particles.

A parallel development of the turnstile mechanism for the TIME method is, however, possible by recognizing the nature of the TIME method and realizing the meaning of the Lagrangian transport boundary  $\mathcal{W}^b(t)$ . It requires the following modification to  $R^H(t)$  as follows, where  $R^H(t)$  is defined in (25) along  $\bar{W}^H$ . In the downstream direction where transport has happened and  $\bar{W}^H$  corresponds to  $\mathcal{W}^S(t)$  associated with the downstream DHT,  $\mathcal{W}^U(t)$  should

correspond to  $R^H(t)$ . In the upstream direction where transport is yet to happen and  $\overline{W}^H$  corresponds to  $\mathcal{W}^U(t)$  associated with the upstream DHT, however,  $\mathcal{W}^S(t)$  should correspond to the mirror image of  $R^H(t)$ :

$$R^\otimes(t) = \{(l, r) | r = -r^H(l, t)\} \quad (49)$$

see Figure 9, in comparison with Figure 2. Table 4 gives the summary of the definitions below.

[Fig.9]

[Tab.4]

**Pseudo-manifolds.** We define the unstable pseudo-manifold  $W^U(t)$  and stable pseudo-manifold  $W^S(t)$  by the segments of  $\overline{W}^H$ ,  $R^H(t)$ , and  $R^\otimes(t)$  as follows. In the arc-length coordinate,  $W^U(t) = \{(l, r) \mid (l, r^U(l, t))\}$  and  $W^S(t) = \{(l, r) \mid (l, r^S(l, t))\}$  are defined by

$$r^U(l, t) = \begin{cases} 0, & \text{for } l \leq l^H(s^\otimes(t)) \text{ on } \overline{W}^H \\ r^H(l, t), & \text{for } l >^H(s^\otimes(t)) \text{ on } R^H(t) \end{cases} \quad (50a)$$

$$r^S(l, t) = \begin{cases} -r^H(l, t), & \text{for } l \leq l^H(s^\otimes(t)) \text{ on } R^\otimes(t) \\ 0, & \text{for } l > l^H(s^\otimes(t)) \text{ on } \overline{W}^H \end{cases}, \quad (50b)$$

where definition of  $s^\otimes(t)$  is given below. The distance  $r^U(t) - r^S(t)$  between  $W^U(t)$  and  $W^S(t)$  is  $r^H(t)$  by these definitions. It also corresponds to  $r^L(l^H(s), t)$  of the Lagrangian transport (45b).

**Pseudo-boundary PIP.** We select  $s^\otimes(t)$  to be

$$s^\otimes(t) \sim s^b(t) \quad (51)$$

out of all the existing  $\{s_j^H(t)\}$  so that the resulting  $W^U(t)$  and  $W^S(t)$  are geometrically closest to their corresponding Lagrangian invariant manifolds  $\mathcal{W}^U(t)$  and  $\mathcal{W}^S(t)$ . This choice of  $s^\otimes(t)$  implies large  $|\mathbf{u}(\mathbf{x}^H(s^b(t)))|$  from (48b) and hence small  $|r^H(l^H(s^\otimes(t)), t)|$ .

**Pseudo-Lagrangian lobes.** Originally the pseudo-lobes are defined for  $C$  in Section 4.2 by the segments of  $R^C(t)$  and  $C$ . For transport dynamics across  $\overline{W}^H$ , however, we follow the convention of the Lagrangian lobes defined in Section B.1. The pseudo-Lagrangian lobe is defined by segments of  $W^U(t)$  and  $W^S(t)$  between a pair of adjacent pseudo-PIPs corresponding to  $s_j^H(t)$  and  $s_{j+1}^H(t)$ . We classify them into two types,  $L^{US}$  or  $L^{SU}$ , depending on whether the corresponding segment of  $W^U(t)$  lies to the left or to the right of the corresponding segment of  $W^S(t)$  in the forward direction of  $s$  along the boundary  $\overline{W}^H$ . Table 2 was computed by following this convention.

Directionality of transport across  $\overline{W}^H$  by the pseudo-Lagrangian lobes. Like Lagrangian lobe dynamics, the relative position of  $s_j^H(t)$  with respect to  $s^\otimes(t)$  determines whether or not the  $j$ -th pseudo-Lagrangian lobe has been transported across  $\overline{W}^H$ . This leads to a further classification of pseudo-Lagrangian lobes,  $L^{(H=)US}$  and  $L^{US(=H)}$  for  $L^{US}$  as well as  $L^{(H=)SU}$  and  $L^{SU(=H)}$  for  $L^{SU}$ . The pseudo-Lagrangian lobes of  $L^{(H=)US}$  and  $L^{SU(=H)}$  lie before  $s^\otimes(t)$  and will cross  $\overline{W}^H$  in the future  $\tau > t$ . In contrast, the pseudo-Lagrangian lobes of  $L^{US(=H)}$  and  $L^{(H=)SU}$  lie after  $s^\otimes(t)$  and have crossed  $\overline{W}^H$  in the past  $\tau < t$ .

**Discrete transport time sequence of TIME.** As in the case of the boundary PIP  $s^b(t)$ , the inverse pseudo-PIPs  $s^\otimes(t)$  also forms a discrete time sequence  $\{t_k^\otimes\}$ . By the construction of  $s^\otimes(t)$  (51),  $\{t_k^\otimes\}$  is an approximation of the discrete time sequence of the boundary PIPs  $\{t_k^b\}$ , i.e.,  $t_k^\otimes \sim t_k^b$  up to leading order.

**Turnstile mechanism of the pseudo-Lagrangian lobes.** Like the Lagrangian lobe dynamics, at the discrete time sequence  $\{t_k^b\}$ , a total of  $\Delta j_k^\otimes - 1$  pseudo-Lagrangian lobes go across  $\overline{W}^H$  into the other region. Therefore, the lobes of  $L^{(H=)SU}$  turn into  $L^{US(=H)}$  and those of  $L^{(H=)US}$  turn into  $L^{SU(=H)}$ . This is the so-called pseudo-turnstile mechanism of the TIME method.

## References

- [1] S. Wiggins, The dynamical systems approach to Lagrangian transport in oceanic flows, *Ann. Rev. Fluid Mech.* 37 (2005) 295–328.
- [2] R. Samelson, S. Wiggins, *Lagrangian Transport in Geophysical Jets and Waves: The Dynamical Systems Approach*, Springer-Verlag, New York, 2006.
- [3] S. Wiggins, K. Ide, Eulerian transport in two classes of three-dimensional geophysical flows, in preparation.
- [4] K. Ide, S. Wiggins, Transport induced by mean-eddy interaction: Ii. diagnostics of transport process, *Physica D*.
- [5] K. Ide, D. Small, S. Wiggins, Distinguished hyperbolic trajectories in time dependent fluid flows: Analytical and computational approach for velocity fields defined as data sets, *Nonl. Proc. Geophys.* 9 (2002) 237–266.
- [6] F. M. A. Salam, The Melnikov technique for highly dissipative systems, *SIAM J. Appl. Math.* 47 (1987) 232–243.
- [7] B. O. Greenspan, P. J. Holmes, Homoclinic orbits, subharmonics and global bifurcation in forced oscillations, in: G. Barenhalt (Ed.), *Nonlinear Dynamcis and Turbulence*, Pitman, Bostron MA, 1983, pp. 172–214.
- [8] J. Guckenheimer, P. J. Holmes, *Nonlinear Oscillations, Dynamical Systems and Bifurcations of the Vector Field*, Springer-Verlag, 1983.
- [9] V. I. Arnold, *Mathematical methods of classical mechanics*, 2nd Edition, Springer-Verlag, 1989.
- [10] V. Rom-Kedar, A. Leonard, S. Wiggins, An analytical study of transport, mixing and chaos in an unsteady vortical flow, *J. Fluid Mech.* 214 (1990) 397–394.
- [11] S. Wiggins, *Chaotic transport in dynamical systems*, Springer-Verlag, Berlin, 1992, 301pp.
- [12] C. Rowley, A modeling study of the North Atlantic Current, Ph.D. thesis, University of Rhode Island (1996).
- [13] H. A. Dijkstra, *Nonlinear Physical Oceanography A Dynamical Systems Approach to the Large Scale Ocean Circulation and El Nino*, 2nd Edition, Springer, 2005.
- [14] E. Simonnet, M. Ghil, K. Ide, R. Temam, S. Wang, Low-frequency variability in shallow-water models of the wind-driven ocean circulation. part ii: Time-dependent solutions, *J. Phys. Oceanogr.* 33 (2003) 729–752.
- [15] C. Coulliette, S. Wiggins, Intergyre transport in a wind-driven, quasigeostrophic double gyre: An application of lobe dynamics, *Nonl. Proc. Geophys.* 7 (2000) 59–85.

- [16] E. Hovmöller, The trough and ridge diagram, *Tellus* 1 (1949) 62–66.
- [17] O. Martis, C. Schwierz, H. C. Davies, A refined Hovmöller diagram, *Tellus* 58A (2006) 221–226.
- [18] A. Mancho, D. Small, S. Wiggins, A tutorial on dynamical systems concepts applied to Lagrangian transport in oceanic flows defined as finite time data sets: Theoretical and computational issues, *Phys. Rep.* 437 (2006) 55–124.
- [19] V. K. Mel’nikov, On the stability of the center for time peridodic perturbations, *Trans. Moscow Math. Soc.* 12 (1963) 1–57.
- [20] P. J. Holmes, Averaging and chaotic motions in forced oscillations, *SIAM J. Appl. Math.* 38 (1980) 65–80.
- [21] F. M. A. Salam, J. E. Marseden, P. P. Varaiya, Chaos and arnold diffusion in dynamical systems, *IEEE Trans. Circuits and Systems CAS-30* (1983) 697–708.
- [22] F. M. A. Salam, S. S. Sastry, Dynamics of the forced josephon junction circuit, *IEEE Trans. Circuits and Systems CAS-32* (1985) 784–796.
- [23] N. Malhotra, S. Wiggins, Geometric structures, lobe dynamics, and Lagrangian transport in flows with aperiodic time dependence, with applications to Rossby wave flow, *J. Nonl. Sci.* 8 (1998) 401–456.



## List of Tables

1	Glossary of TIME functions. See text for details.	36
2	Quantitative comparison of transport by the TIME pseudo-Lagrangian lobes using the pseudo-manifold described in Appendix B and by the Lagrangian lobes using the method described in [15] at $t_{944}^*$ (see Figure 3b for the lobe number). Results of the TIME pseudo-Lagrangian lobes are based on the pseudo-manifolds described in Appendix B. The signed area of a pseudo-lobe and a Lagrangian lobe corresponds to the amount of transport: a positive value represents transport from the subpolar gyre to the subtropical gyre, while a negative value represents transport from the subtropical gyre to the subpolar gyre.	37
3	A general comparison between the TIME method and Lagrangian method.	38
4	Relation between the TIME method and Lagrangian lobes for transport associated with $\bar{W}^H$ . For (pseudo-)lobe type, “right to left” and “left to right” indicate the direction of transport while “future” and “past” indicate the timing of transport with respect to the present time $t$ . See text for details.	39

## List of Figures

- 1 Geometry associated with the TIME method: a) Eulerian boundary  $C = \{\bar{\mathbf{x}}^C(s)\}$  and the mean velocity  $\overline{\mathbf{u}}(\mathbf{x})$ ; b) instantaneous flux  $\phi(\mathbf{x}, t)$  across  $C$  as the parallelogram in the unsteady flow; c) accumulation  $m^C(s, t; D)$  (the shaded portion represents the accumulation); d) displacement distance  $m^C(s, t; D)$  (the shaded area represents a positive pseudo-lobe area). 40
- 2 Schematics of pseudo-lobes along  $C$ : a) in  $\mathbf{x}$ ; b) in  $(l, r)$ ; c) in  $(s, m)$ . The shaded areas correspond to the net accumulation of fluid particles originally on the right side of  $C$ , where the direction is defined with respect to the direction of increasing  $s$ , which accumulated onto the left side of  $C$  at time  $t$ . 41
- 3 Double-gyre circulation: a) streamfunction  $\psi(\mathbf{x}, t)$  at  $t = t_{944}^*$ ; b) unstable manifold  $\mathcal{W}^U(t)$  (solid line) and stable manifold  $\mathcal{W}^s(t)$  (dashed line) of the inter-gyre transport by the Lagrangian method; and c) reference streamfunction  $\bar{\psi}(\mathbf{x})$  and the Eulerian boundary  $\bar{W}^H = \bar{\mathbf{x}}^H(s)$  of the inter-gyre transport by the TIME method. In (a) and (c), contour interval 2000 with dash lines for negative values. In (b), numbers correspond to those in Table 2 In (c),  $\bar{W}^H = \bar{\mathbf{x}}^H(s)$  is the thick solid line with four white circles plotted at every 250 days starting from in  $s = 0$ , i.e.,  $\bar{\mathbf{x}}^H(s_0^*)$ ,  $\bar{\mathbf{x}}^H(s_{250}^*)$ ,  $\bar{\mathbf{x}}^H(s_{500}^*)$ , and  $\bar{\mathbf{x}}^H(s_{1000}^*)$ ; the diamonds at  $\bar{\mathbf{x}}^H(s_J)$ ,  $\bar{\mathbf{x}}^H(s_N)$ , and  $\bar{\mathbf{x}}^H(s_S)$ , with  $(s_J, s_N, s_S) = (s_{110}^*, s_{129}^*, s_{174.5}^*)$ ;  $\bar{\mathbf{x}}^H(s_J)$  almost overlaps  $\bar{\mathbf{x}}^H(s_0^*)$ . 42
- 4 The instantaneous flux function  $\mu^H(s, t)$  in the Hovmöller diagram with dash-dot line for the negative values and contour interval  $40\text{km}^2/\text{day}$ . The diagonal line is an example of reference trajectory going through  $(s_0, t_0) = (0, 1300)$ . The horizontal lines corresponds to the four phases during one period of the oceanic oscillation, at  $t = t_{944}^*, t_{944}^* + T/4, t_{944}^* + T/2, t_{944}^* + 3T/4$ . 43
- 5 The instantaneous flux function  $\mu^H(s, t)$  at  $t = t_{944}^*, t_{944}^* + T/4, t_{944}^* + T/2, t_{944}^* + 3T/4$  from bottom to top (right) with corresponding time indicated in Figure 4. 44

- 6 The accumulation functions  $a^H(s, t)$  (dash line),  $a^U(s, t; t)$  (solid line), and  $a^S(s, t; t)$  (dash-dot line) at  $t_{944}^*$ ,  $t_{982}^*(= t_{944}^* + T/4)$ ,  $t_{1020}^*(= t_{944}^* + T/2)$ , and  $t_{1058}^*(= t_{944}^* + 3T/4)$  (from bottom to top) with corresponding time indicated in Figure 4:  $a^H(s, t)$  almost overlaps  $a^S(s, t; t)$  for  $s < s_J$  and  $a^U(s, t; t)$  for  $s > s_S$ . 45
- 7 The displacement distance functions,  $r^H(l, t)$  (dash line),  $r^U(l, t; t)$  (solid line), and  $r^S(l, t; t)$  (dash-dot line) at  $t_{944}^*$  corresponding to the bottom panel in Figure 6;  $r^H(l, t)$  almost overlaps  $r^S(l, t; t)$  for  $l < l^H(s_J)$  and  $r^U(s, t; t)$  for  $l < l^H(s_S)$ , although pseudo-lobes of  $r^H(l, t)$  and  $r^U(l, t; t)$  accumulate near  $l = 0$  and cannot be seen in this figure. 46
- 8 Schematics of Lagrangian lobes in  $\mathbf{x}$ . The shaded lobe  $\mathcal{L}_{j+2, j+3}^{US(=b)}(t)$  corresponds to fluid particles which have already transported from the right to the left of the deformable Lagrangian boundary  $\mathcal{W}^b(t)$ , while the swatched lobe  $\mathcal{L}_{j, j+1}^{(b=)US}(t)$  corresponds to fluid particles to be transported in the future time. 47
- 9 Schematics of pseudo-Lagrangian lobe in a)  $\mathbf{x}$  and b)  $(l, r)$ . The shaded pseudo-Lagrangian lobe  $L_{j+2, j+3}^{US(=H)}(t)$  corresponds to net amount of fluid particles which have already been transported from the right to the left of  $\overline{W}^H$ , while the swatched lobe  $L_{j, j+1}^{(H=)US}(t)$  corresponds to the net amount of fluid particles to be transported in the future time. 48

Symbol	Definition	Equations
$s$	flight-time coordinate along $C$	(4)
$C = \{\bar{\mathbf{x}}^C(s)\}$	Eulerian boundary over the segment $s \in [s_a, s_b]$ , including:	(4)
	$\overline{W}^S$ semi-infinite for $s \in [s_0, \infty)$	(6)
	$\overline{W}^U$ semi-infinite for $s \in (-\infty, s_0]$	(6)
	$\overline{W}^H$ bi-infinite for $s \in (-\infty, \infty)$	(7)
$(s, t) = (s_0 - t_0 + t, t)$	reference particle trajectory (advection) along $C$	(5)
$(l, r) = (l^C(s), r)$	arc-length coordinate in two dimensions	(8)
$m^C(s, t; t_0 : t_1)$	accumulation function	(14),(19)-(21)
$a^C(s, t; t_0 : t_1)$	displacement area function	(15),(19)-(21)
$r^C(s, t; t_0 : t_1)$	displacement distance function	(15),(19)-(21)
$s_j^C(t)$	pseudo-PIP	(26)
$L_{j,j+1}^C(t)$	pseudo-lobe, which belongs to the following two types:	(28)
	$L^{RC}$ from right to left across $C$	
	$L^{CR}$ from left to right across $C$	
$A(L_{j,j+1}^C(t))$	signed area of pseudo-lobe	(29)

Table 1

Glossary of TIME functions. See text for details.

	TIME	Lagrangian
lobe no id. ( $j$ )	$A(L_{j,j+1}^H(t_B))$ (km <sup>2</sup> )	$\mathcal{A}(\mathcal{L}_{j,j+1}^L(t_B))$ (km <sup>2</sup> )
1	6858	6258
2	-6776	-6355
3	6796	6201
4	-6783	-6216
5	6760	6424
6	-6838	-6515
7	6819	6696
8	-6811	-6119

Table 2

Quantitative comparison of transport by the TIME pseudo-Lagrangian lobes using the pseudo-manifold described in Appendix B and by the Lagrangian lobes using the method described in [15] at  $t_{944}^*$  (see Figure 3b for the lobe number). Results of the TIME pseudo-Lagrangian lobes are based on the pseudo-manifolds described in Appendix B. The signed area of a pseudo-lobe and a Lagrangian lobe corresponds to the amount of transport: a positive value represents transport from the subpolar gyre to the subtropical gyre, while a negative value represents transport from the subtropical gyre to the subpolar gyre.

		TIME	Lagrangian
type		particle, flow property $Q$	particle
boundary	spatial	any reasonable $C$	$\mathcal{W}^b(t)$ only
	temporal	stationary	continuously deformable & discontinuous at $\{t_k^b\}$
$\mathbf{u}(\mathbf{x}, t)$	restriction	$ \mathbf{u}'(\mathbf{x}, t) $ small along $C$	no restriction
	spatial requirement	along $C$ only	non-local in $\mathbf{x}$
	temporal period	flexible	infinite
transport process	temporal	continues	turnstile at $\{t_k^b\}$
	spatial	all along $C$	locally near $\mathbf{x}^b(l^b(t_k^b), t_k^b)$
computation		efficient	exhaustive
accuracy		leading order	accurate

Table 3

A general comparison between the TIME method and Lagrangian method.

			TIME	Lagrangian
geometry	intersection sequence		$\{s_j^H(t)\}$	$\{s_j^L(t)\}$
	distance		$r^H(l, t)$	$r^L(l, t)$
	area		$A(L_{j,j+1}^H(t))$	$\mathcal{A}(\mathcal{L}_{j,j+1}^L(t)) \approx A(\mathcal{L}_{j,j+1}^L(t))$
transport by turnstile	boundary point		$s^\otimes(t)$	$s^b(t)$
	time sequence		$\{t_k^\otimes\}$	$\{t_k^b\}$
	lobe number		$j_k^\otimes$	$j_k^b$
	lobe increment		$\Delta j_k^\otimes$	$\Delta j_k^b$
(pseudo-)	right	future	$L^{(H=)US}$	$\mathcal{L}^{(b=)US}$
lobe	to left	past	$L^{US(=H)}$	$\mathcal{L}^{US(=b)}$
type	left	future	$L^{SU(=H)}$	$\mathcal{L}^{SU(=b)}$
	to right	past	$L^{(H=)SU}$	$\mathcal{L}^{(b=)SU}$

Table 4

Relation between the TIME method and Lagrangian lobes for transport associated with  $\overline{W}^H$ . For (pseudo-)lobe type, “right to left” and “left to right” indicate the direction of transport while “future” and “past” indicate the timing of transport with respect to the present time  $t$ . See text for details.

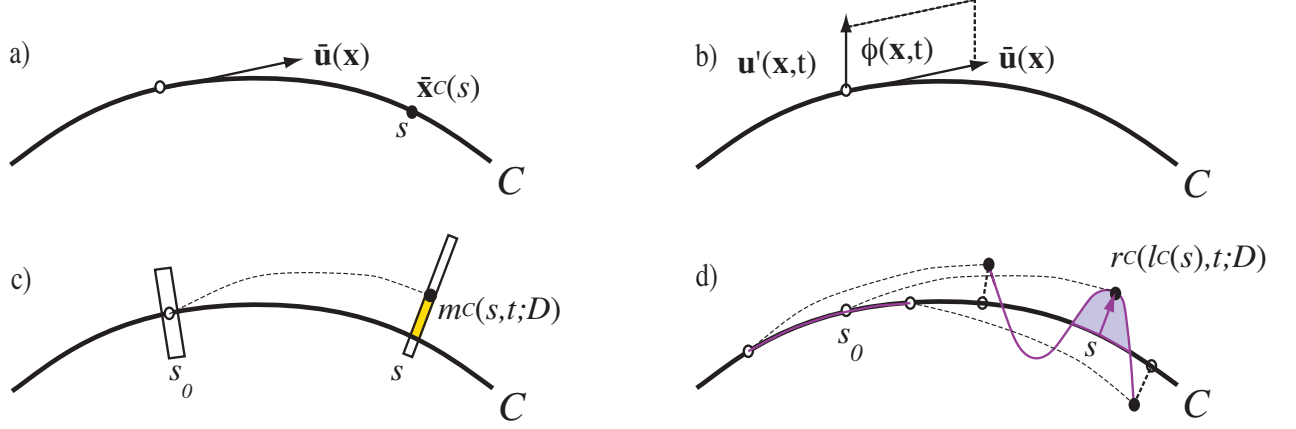


Fig. 1. Geometry associated with the TIME method: a) Eulerian boundary  $C = \{\bar{\mathbf{x}}^C(s)\}$  and the mean velocity  $\bar{\mathbf{u}}(\mathbf{x})$ ; b) instantaneous flux  $\phi(\mathbf{x},t)$  across  $C$  as the parallelogram in the unsteady flow; c) accumulation  $m^C(s,t;D)$  (the shaded portion represents the accumulation); d) displacement distance  $m^C(s,t;D)$  (the shaded area represents a positive pseudo-lobe area).



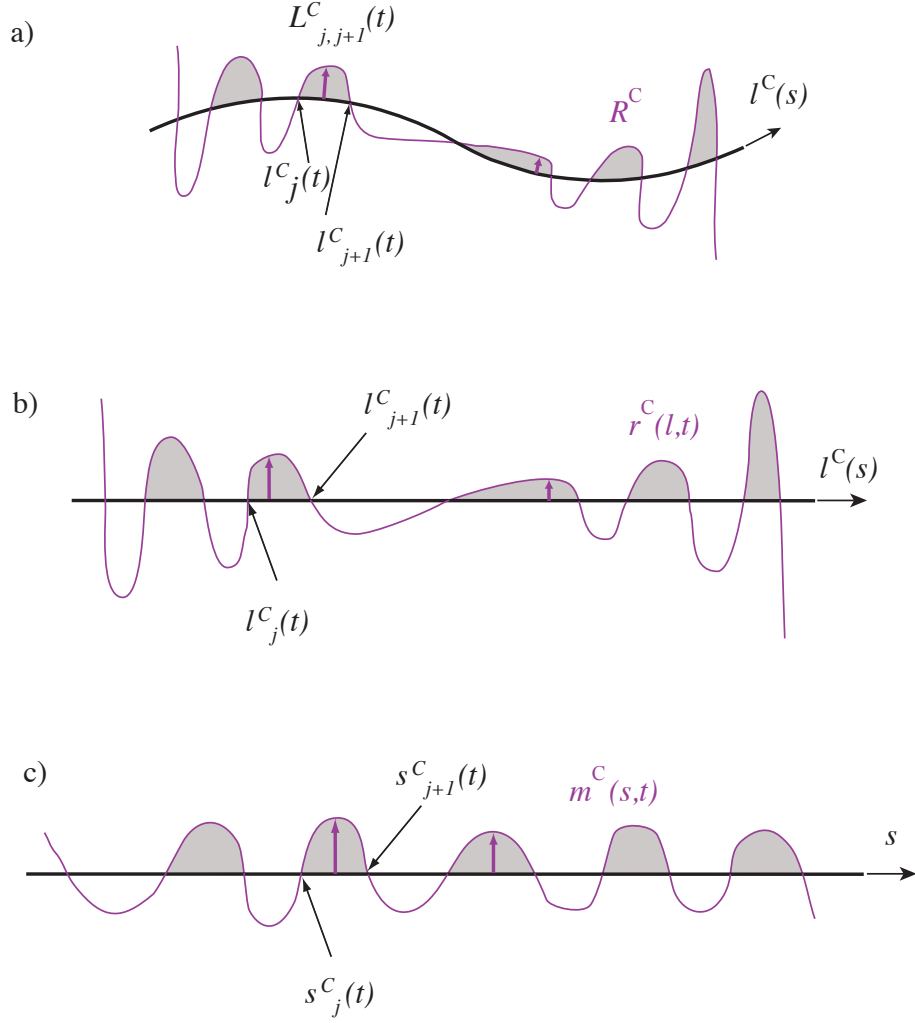


Fig. 2. Schematics of pseudo-lobes along  $C$ : a) in  $\mathbf{x}$ ; b) in  $(l, r)$ ; c) in  $(s, m)$ . The shaded areas correspond to the net accumulation of fluid particles originally on the right side of  $C$ , where the direction is defined with respect to the direction of increasing  $s$ , which accumulated onto the left side of  $C$  at time  $t$ .

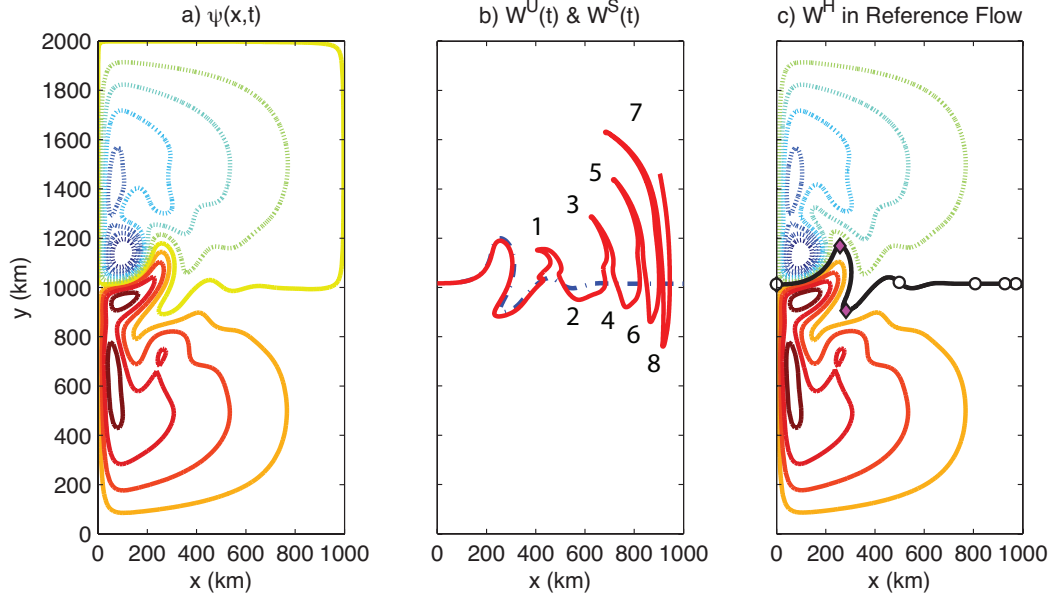


Fig. 3. Double-gyre circulation: a) streamfunction  $\psi(\mathbf{x}, t)$  at  $t = t_{944}^*$ ; b) unstable manifold  $W^U(t)$  (solid line) and stable manifold  $W^S(t)$  (dashed line) of the inter-gyre transport by the Lagrangian method; and c) reference streamfunction  $\bar{\psi}(\mathbf{x})$  and the Eulerian boundary  $\bar{W}^H = \bar{x}^H(s)$  of the inter-gyre transport by the TIME method. In (a) and (c), contour interval 2000 with dash lines for negative values. In (b), numbers correspond to those in Table 2. In (c),  $\bar{W}^H = \bar{x}^H(s)$  is the thick solid line with four white circles plotted at every 250 days starting from in  $s = 0$ , i.e.,  $\bar{x}^H(s_0^*)$ ,  $\bar{x}^H(s_{250}^*)$ ,  $\bar{x}^H(s_{500}^*)$ , and  $\bar{x}^H(s_{1000}^*)$ ; the diamonds at  $\bar{x}^H(s_J)$ ,  $\bar{x}^H(s_N)$ , and  $\bar{x}^H(s_S)$ , with  $(s_J, s_N, s_S) = (s_{110}^*, s_{129}^*, s_{174.5}^*)$ ;  $\bar{x}^H(s_J)$  almost overlaps  $\bar{x}^H(s_0^*)$ .

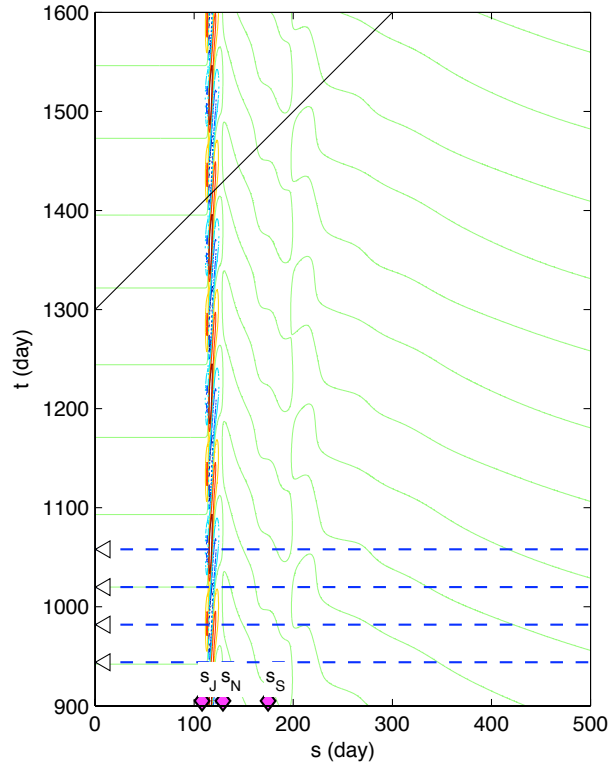


Fig. 4. The instantaneous flux function  $\mu^H(s, t)$  in the Hovmöller diagram with dash-dot line for the negative values and contour interval  $40\text{km}^2/\text{day}$ . The diagonal line is an example of reference trajectory going through  $(s_0, t_0) = (0, 1300)$ . The horizontal lines corresponds to the four phases during one period of the oceanic oscillation, at  $t = t_{944}^*, t_{944}^* + T/4, t_{944}^* + T/2, t_{944}^* + 3T/4$ .

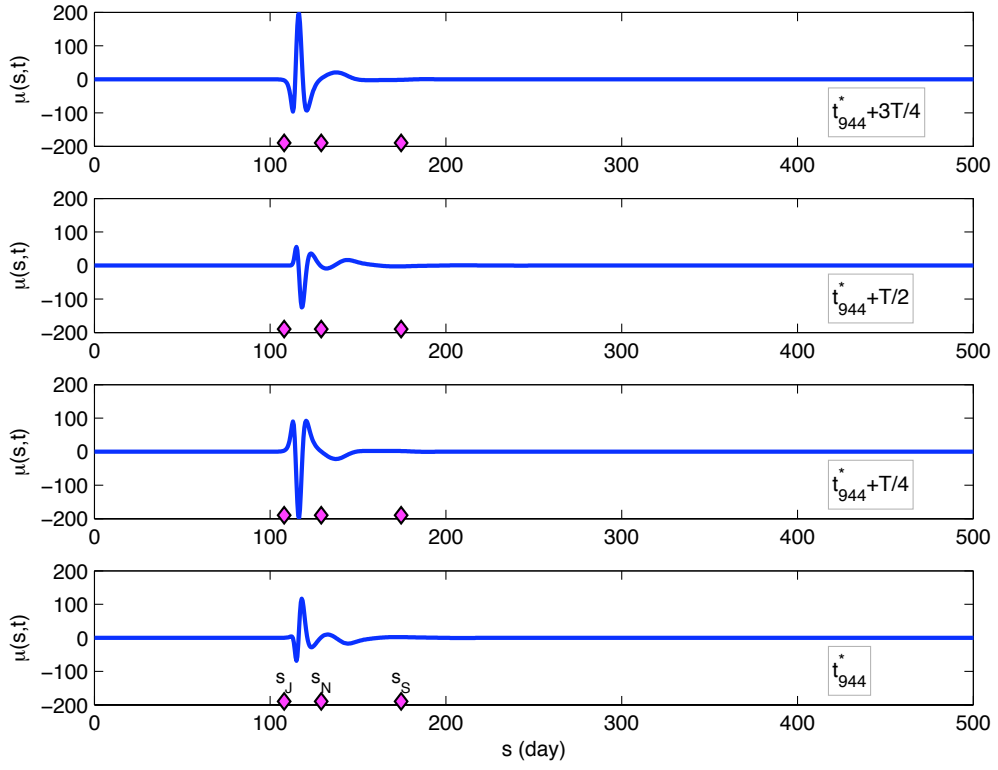


Fig. 5. The instantaneous flux function  $\mu^H(s, t)$  at  $t = t_{944}^*, t_{944}^* + T/4, t_{944}^* + T/2, t_{944}^* + 3T/4$  from bottom to top (right) with corresponding time indicated in Figure 4.

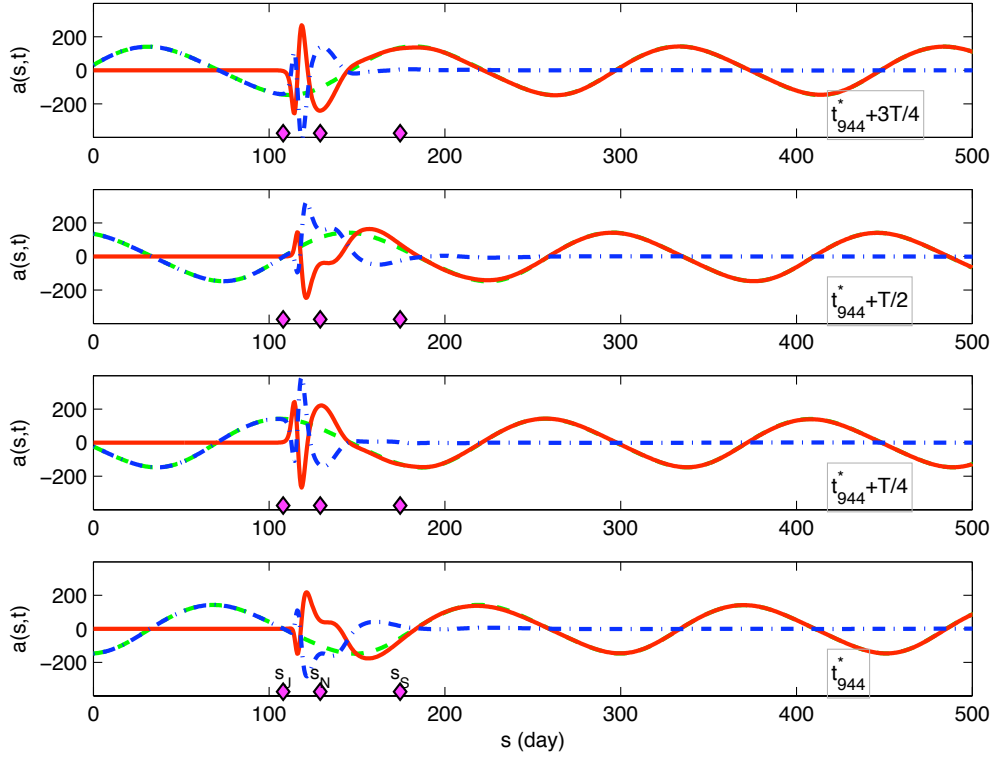


Fig. 6. The accumulation functions  $a^H(s, t)$  (dash line),  $a^U(s, t; t)$  (solid line), and  $a^S(s, t; t)$  (dash-dot line) at  $t_{944}^*$ ,  $t_{982}^*(= t_{944}^* + T/4)$ ,  $t_{1020}^*(= t_{944}^* + T/2)$ , and  $t_{1058}^*(= t_{944}^* + 3T/4)$  (from bottom to top) with corresponding time indicated in Figure 4:  $a^H(s, t)$  almost overlaps  $a^S(s, t; t)$  for  $s < s_J$  and  $a^U(s, t; t)$  for  $s > s_S$ .

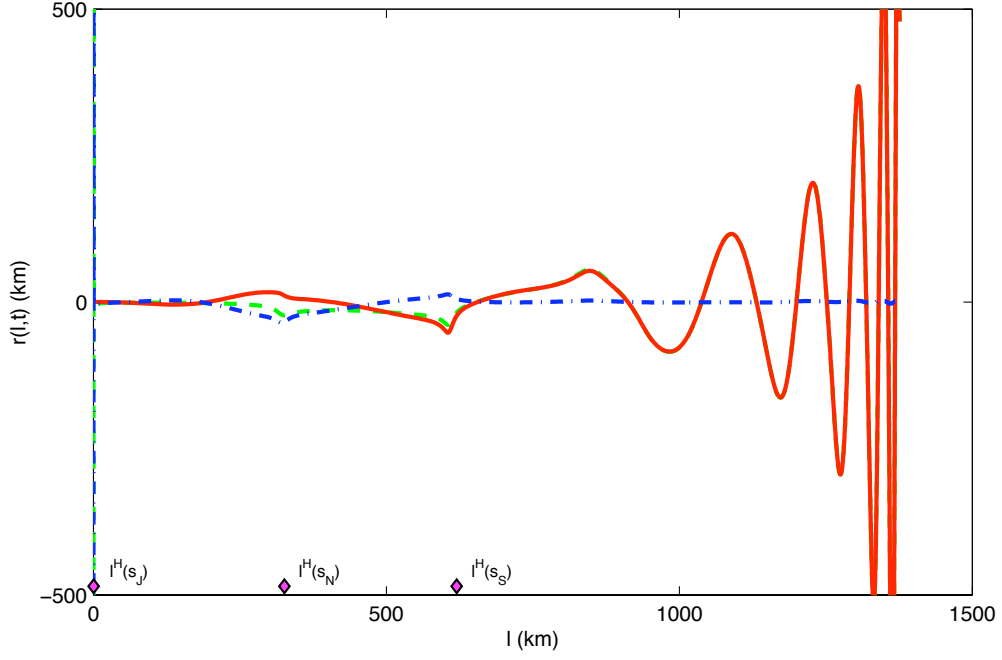


Fig. 7. The displacement distance functions,  $r^H(l, t)$  (dash line),  $r^U(l, t; t)$  (solid line), and  $r^S(l, t; t)$  (dash-dot line) at  $t_{944}^*$  corresponding to the bottom panel in Figure 6;  $r^H(l, t)$  almost overlaps  $r^S(l, t; t)$  for  $l < l^H(s_J)$  and  $r^U(s, t; t)$  for  $l < l^H(s_S)$ , although pseudo-lobes of  $r^H(l, t)$  and  $r^U(l, t; t)$  accumulate near  $l = 0$  and cannot be seen in this figure.

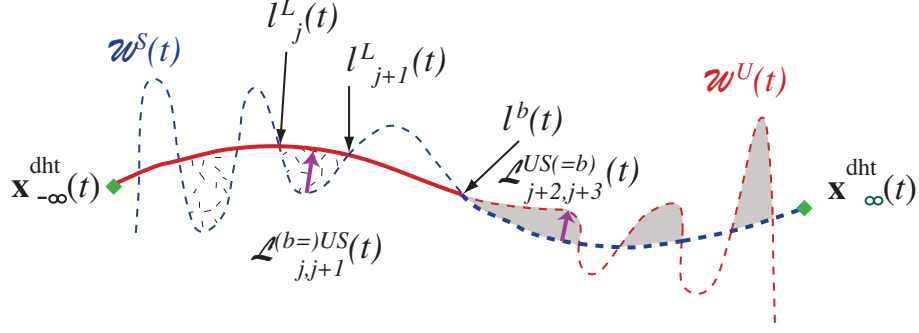


Fig. 8. Schematics of Lagrangian lobes in  $\mathbf{x}$ . The shaded lobe  $\mathcal{L}^{US(=b)}_{j+2,j+3}(t)$  corresponds to fluid particles which have already transported from the right to the left of the deformable Lagrangian boundary  $\mathcal{W}^b(t)$ , while the swatched lobe  $\mathcal{L}^{(b=)US}_{j,j+1}(t)$  corresponds to fluid particles to be transported in the future time.

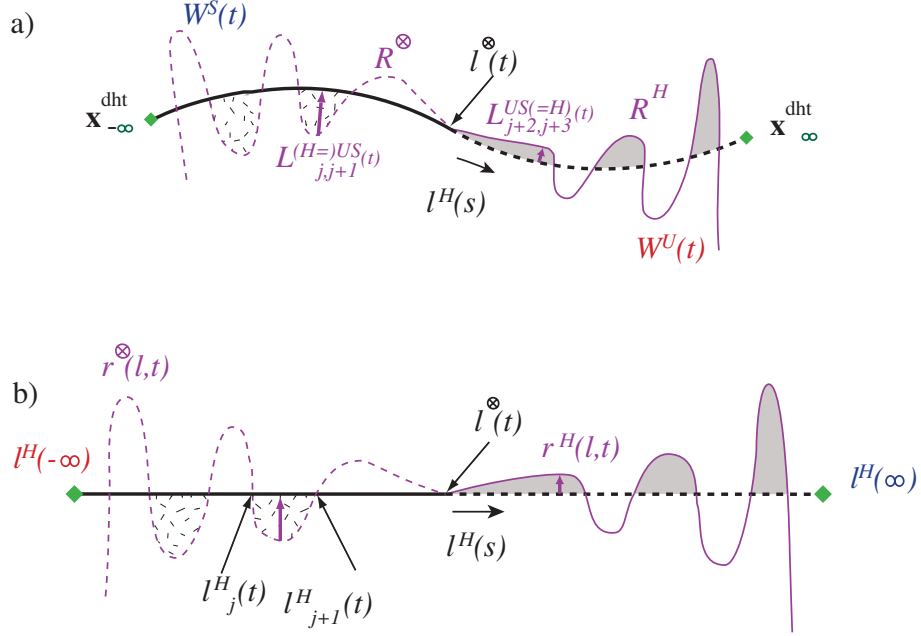


Fig. 9. Schematics of pseudo-Lagrangian lobe in a)  $\mathbf{x}$  and b)  $(l, r)$ . The shaded pseudo-Lagrangian lobe  $L_{j+2,j+3}^{US(=H)}(t)$  corresponds to net amount of fluid particles which have already been transported from the right to the left of  $\overline{W}^H$ , while the swatched lobe  $L_{j,j+1}^{(H=)US}(t)$  corresponds to the net amount of fluid particles to be transported in the future time.